Vibratory Stress Relief in Manufacturing the Rails of a Maglev System

Delin Rao, Jingguo Ge, and Ligong Chen

Department of Material Engineering, Shanghai Jiaotong University, Shanghai, P.R. China

To reduce the welding induced residual stress in the rails of a magnetic levitation (maglev) transport system, the procedure of vibratory stress relief (VSR) is applied and discussed in this paper. Suitable welding sequence for the rails is introduced to keep the residual stress low. Qualitative analysis with scanning curve shows that the peak of acceleration becomes higher after the procedure of VSR and the resonant frequency becomes lower. It means that the procedure of VSR is effective according to the JB/T5926-91 standard. The residual stress in the rail was measured before VSR and after VSR, using hole-drilling method, and the result shows that the average principal stresses was reduced by about 30% after VSR. [DOI: 10.1115/1.1644544]

Introduction

The first magnetic levitation transport system (maglev system) in China is being built in Shanghai, China's largest commercial center. When completed, it will take only 8 minutes for passengers on the maglev line trains to travel 30 kilometers between Pudong International Airport and the city center. To keep the maglev train at high speed and comfortable, the manufacturing of the rails is very important. This route consists of more than 20,000 pieces of rails. Each rail is 3 meters long and is welded together with StE355 steel and MSH steel using CO_2 shield arc welding. The welding processes will induce a state of residual stress that causes the distortion of the rail. As the permitted tolerance is less than 1mm along the traverse direction, the residual stress after welding must be relieved in order to maintain the dimensional stability.

The commonly used method of stress relief is heat treatment, or annealing, which is effective in many cases. But in maglev case, the component is so large that heat treatment is not feasible due to the size of the furnace and the cost of treatment. The other disadvantage of the heat treatment is the growth of oxides on the component surface. The rail is sprayed with aluminum coating to resist the corrosion. Heat treatment at high temperature will inevitably destroy this coating. Heat treatment entails uniform heating of the component, holding at certain temperature, and then a controlled cooling. Thus the procedure is time consuming which cannot meet

the schedule of maglev manufacturing. It is obvious that procedure of heat treatment to reduce residual stress is impractical in manufacturing the rails for the maglev system.

Vibratory Stress Relief (VSR)

One kind of mechanical methods of stress relief is vibration-vibratory stress relief (VSR). The vibration is created by an eccentric mass electric motor which is attached to the component. The basic theory is that the cyclic vibratory stresses added to the residual stresses exceed the yield strength of the material and causes local plastic deformation and substantial reduction of residual stresses [1,2,3]. Components subjected to the VSR treatment range in mass from a few kilograms to several hundred tones. The bigger the component is, the easier the treatment is. Oxidation of the component surface does not happen as the VSR works at room temperature. The amount of time that the component subjected to the vibration usually depends on its weight and generally is less than 20 minutes. Because of such advantages of VSR, it is used in manufacturing the rail of maglev line.

Four beams are welded to form the rail. Two materials are used. The mechanical properties of the two steels are listed in Table 1.

Welding and VSR Procedure

The cross-section of the rail is close to rectangular. Suitable welding sequence will induce low-level residual stress in the rail. The assembling and welding sequence is shown in Fig. 1

To reduce the welding deformation, straightening with manual local heating is carried out after the first three beams are welded. When the fourth beam is welded, straightening is carried out again before the VSR process. An eccentric mass electric motor is attached to one end of the rail. Rigid clamps are used to integrate the motor and the rail. The rail is supported on rubber isolator as it must be allowed to freely deform during the treatment [4]. The supporting points are beneath the nodal lines of the first mode of vibration. A computer is used to control the running speed of the motor so the vibratory frequency can change. An acceleration sensor mounted on the rail will identify the resonant conditions as the frequency range is scanned. A resonant peak occurs when the induced vibratory frequency of the motor coincides with the rail's natural frequency. The computer records every peak acceleration and frequency. After the scanning the computer keeps the motor running near the frequency of highest peak acceleration for 15–20 minutes [5,6]. The whole VSR procedure is under the automatic control of a computer. A chart recording the detail resonant response and duration of treatment is produced after the VSR.

Residual Stress Measurement

In order to evaluate the effectiveness of VSR, it is necessary to measure the residual stress in the rails. Residual stress is measured with the hole-drilling method [7,8]. The rosette strain gauge, type 120-2CF0-90-45 is used (Fig. 2). The measurement criteria follow JB/T5926-91 standard (Chinese standard).

The hole depth is 2 mm and the drilling rate is 0.2mm/min. According to the welding sequence (Fig. 1), straightening with heat may reduce the residual stress. It is obvious that the highest

Table 1 Ambient mechanical properties of four beams

	Material	Thickness (mm)	Yield stress (MPa)	Ultimate tensile stress (MPa)	Elongation (%)
Beam1,2,3	StE355	20~40	390~420	500~530	33~38
Beam4	MSH	30	390	510	37

level of residual stress occurs on the last weld bead. So the measurement line is on the last weld bead shown in Fig. 4. The position of measurement is subjected to the X.

Two rail specimens are selected and each one has six measurement points along the longitude of weld bead. In order to provide a comparison of residual stresses before VSR and after VSR, two rosette strain gauges are attached to every measurement point. One is used to measure the residual stress before VSR. The other is used after VSR. The distance between the two gauges is 50mm (Fig. 3). It is postulated that the two gauges are at the same position as the rail is 3 meters long.
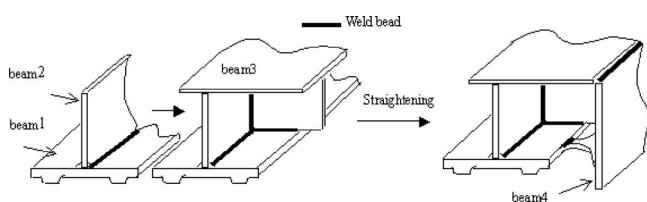

Fig. 1 Welding sequence of the rail
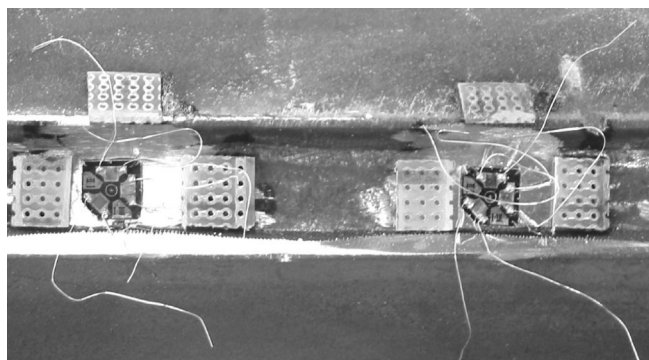

Fig. 2 Field test of VSR

Fig. 3 Rosette strain gauge

Experiment Results

The speed of the motor is converted to the frequency of vibration and recorded using a computer. The sensor of acceleration can record the response of the rail. Then the accelerations, or the responses, are plotted against the vibration frequency, or the excitement. One vibration response of the rail is shown in Fig. 5. Two scanning curves, before VSR and after VSR, are shown in this figure. The difference of speed between two maximum acceleration points is 31.4 rpm while the difference of acceleration is 5.6 m/s^2.

Figure 4 shows that the last weld bead is parallel to the rail. The working rail can be regarded as beam with fixed supported at each end. The longitudinal stress, due to bending and vibrating, is mainly concerned. Quantitative analysis of the VSR effect is based on the measurement result of residual stress. The maximum principal stress and the longitudinal stress, before VSR and after VSR, are shown in Table 2. Figures 6 and 7 plot the change of the residual stress before and after VSR.

Discussion

In vibration analysis, the stress-strain curve will enclose an area, referred to as the hysteresis loop, that is proportional to the energy lost per cycle. Generally speaking, vibration reduces the residual stress of the component, therefore the material (or hysteretic) damping inside the component also decreases. VSR system can be regarded as a damped forced vibration system. The resonant frequency of the system will shift as the material damping
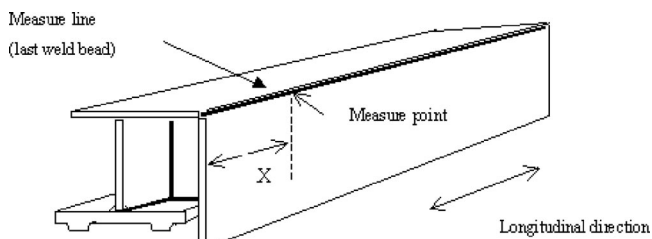

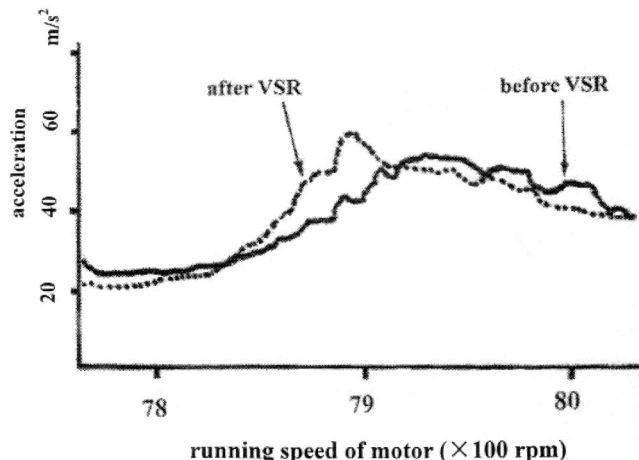**Fig. 4 Measurement line on the weld bead**

Fig. 5 Frequency scanning before VSR and after VSR

Table 2 Maximum principal stress and longitudinal stress on weld bead of rail

	Average maximum principal stress (MPa)		Average longitudinal stress (MPa)	
	Before VSR	After VSR	Before VSR	After VSR
Rail 1	117	83	88	58
Rail 2	135	79	96	57

(a) rail 1   (b) rail 2
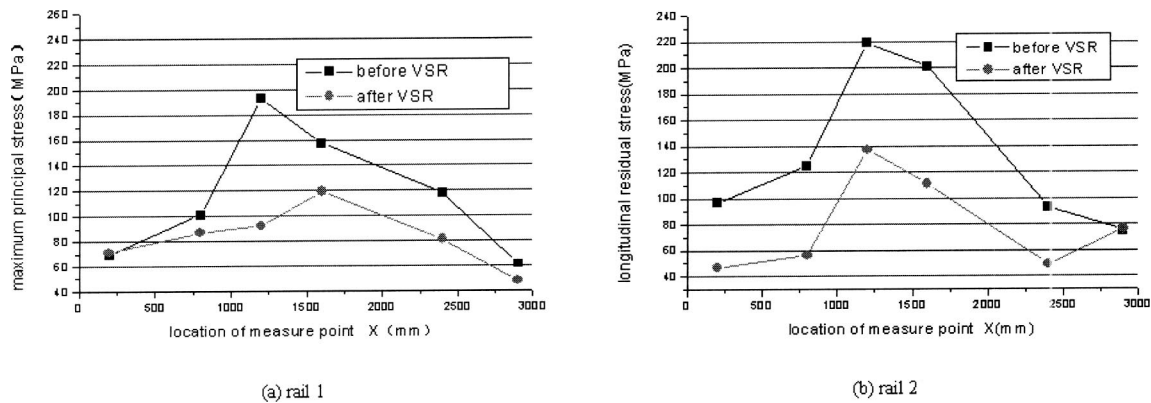
Fig. 6 Maximum principal residual stress before and after VSR

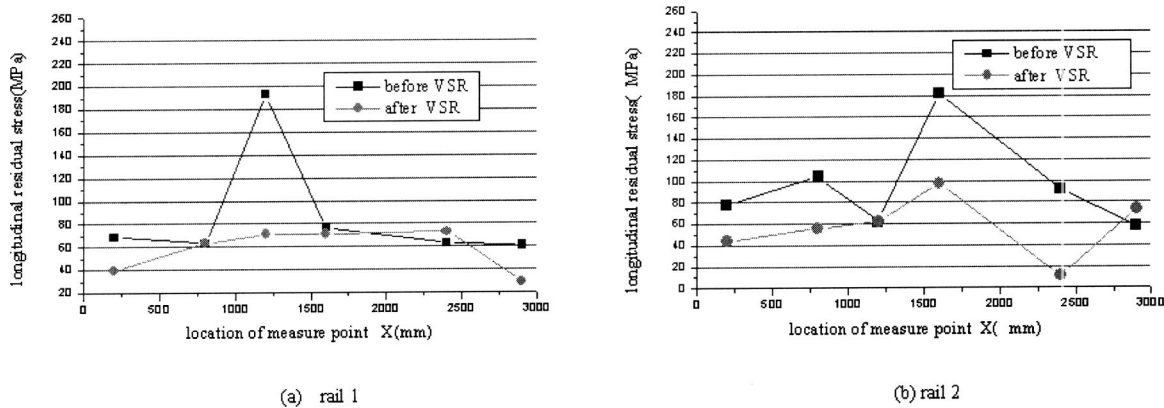
(a) rail 1   (b) rail 2

Fig. 7 Longitudinal residual stress before and after VSR

decreases [9]. This theory can be used to evaluate the result of VSR for qualitative analysis [10]. Two scanning curves before VSR and after VSR are shown in Fig. 5. Before VSR the maximum peak of acceleration and the running speed of motor are 57.6 m/s^2 and 7923.4 rpm respectively. After VSR they become 63.2 m/s^2 and 7892.0 rpm. It shows that the peak of acceleration becomes higher after the procedure of VSR and the resonant frequency becomes lower. Sharper peak appear after VSR. These are coincident with the vibration mechanics. Scanning curve like this means the procedure of VSR is effective according to the JB/T5926-91 standard (Chinese standard).

In Table 1, comparisons are shown between the changing of principal residual stress before VSR and after VSR. As to rail 1, the difference between maximum and minimum principal residual stress equals 287MPa before VSR. After VSR this value becomes 235MPa. As to rail 2, the difference changes from 432MPa to 314MPa. It is observed in Fig. 6 that the maximum principal residual stresses reduce due to the VSR treatment and the redistribution of residual stresses along the weld bead. Before VSR, the average value of principal residual stress of rail 1 is 117MPa, and rail 2 is 135MPa. After VSR, these two values become 83MPa and 79MPa. Thus, the average principal residual stresses reduce by

29% and 41% respectively. Figure 7 provides the distribution of longitudinal residual stress before VSR and after VSR. The average values of longitudinal residual stresses in two rails are 88MPa and 96MPa before VSR. They become 58MPa and 57MPa after VSR. The longitudinal residual stresses reduce by 34% and 40% respectively.

Conclusions

Because of the characteristic of the rail of maglev system, thermal stress relieving (TSR) or annealing is not practical in manufacturing the rail. Vibratory stress relief method is used which avoids the side effects of TSR (distortion, oxidation of surface and degradation of mechanical properties). By comparing two scanning curves before VSR and after VSR, the result of stress relieving is effective according to the JB/T5926-91 standard. The further measurement shows that the average principal stresses reduce by about 30% after VSR. The geometrical form of the rail is controlled in tolerance that is permitted. The procedure of VSR can be used in manufacturing the rail of maglev system effectively.

References

[1] Walker, C. A., Waddell, A. J., and Johnston, D. J., 1995, "Vibratory Stress Relief—An Investigation of the Underlying Processes," Proc. R. Soc. London, Ser. A, **209**, pp. 51–58.

[2] Claxton, R. A., and Lupton, A., 1991, "Vibratory Stress Relieving of Welded Fabrications," Welding & Metal Fabrication, December, pp. 541–544.

[3] G. Gnirss, 1988, "Vibration and Vibratory Stress Relief: Historical Development, Theory and Practical Application," *Welding in the World*, Vol. 26(11–12), pp. 284–291.

[4] Dawson, R., and Moffat, D. G., 1980, "Vibratory Stress Relief: A Fundamental Study of Its Effectiveness," J. Eng. Mater. Technol., **102**, pp. 169–176.

[5] Munsi, A. S. M. Y., Waddell, A. J., and Walker, C. A., 2001, "Modification of Residual Stress by Post-weld Vibration," Mater. Sci. Technol., **17**, May, pp. 601–605.

[6] Wu, Weite, and Lin, Dong-Yih, 1999, "Mechanical Properties of Weldment Affected by Various Vibration Frequencies," J. Mater. Sci. Lett., **18**, pp. 1829–1831.

[7] Middleton, J. C., 2001, "Residual Stress Measurement at Corus, Swinden, Technology Center," Strain, **37**(1), pp. 5–8.

[8] Walker, Donna, 2001, "Residual Stress Measurement Techniques," Advanced Materials & processes, August, pp. 30–33.

[9] Hebel, Thomas, 1986, "A Better Way to Relieve Stress," American Machinist & Automated Manufacturing, December, pp. 70–72.

[10] Yang, Xu, Cai, Sun Mao, Ben, Li Qing, 2002, "Effectiveness Criterion for the In Situ Evaluation of Vibratory Stress Relieving Process," Transactions of the China Welding Institution (Chinese), **23**(2), pp. 66–67.

Monitoring Resistance Spot Nugget Size by Electrode Displacement

D. F. Farson, J. Z. Chen, K. Ely and T. Frech
e-mail: Farson.4@osu.edu

Industrial, Welding and System Engineering Department, The Ohio State University, Columbus, OH 43221

A high-speed video imaging system was employed to directly measure the electrode displacement of the small scale resistance spot welding (SSRSW) process. This measurement technique was chosen because it eliminates a number of potential error sources inherent in other electrode displacement measuring techniques. Careful observation of the heating and cooling portions of the electrode displacement curves revealed that each is comprised of two identifiable segments. Distinct high-velocity segments of the displacement curves were thought to correspond to solid-liquid phase transitions in the weld nugget, while lower-velocity portions corresponded to thermal expansion or contraction of solid material. It was found that the magnitudes of the high speed portions of the electrode displacement were more closely correlated with the weld nugget thickness than was the overall magnitude of the electrode displacement. Furthermore, all measures of electrode displacement were more closely correlated to weld nugget thickness than to nugget diameter. [DOI: 10.1115/1.1644550]

1 Introduction

Although resistance spot welding (RSW) is very widely used in sheet metal joining applications and in small-scale (e.g. electronic and biomedical device) fabrication [1], it is not easy to accurately monitor or control the size of the finished weld nugget. Over the past several decades, process characteristics that have been used for in-process monitoring and control of RSW include current and voltage [2], dynamic resistance [3–7], electrode displacement [8–12], electrode acceleration [13] and force [14–16]. Furthermore, ultrasonic sensing [17], infrared thermography and acoustical emission [18] have also been applied for this purpose. At least two reviews of various weld monitoring techniques have recently been published [19,20]. Artificial intelligence and fuzzy logic algorithms [21–23] as well as simpler linear PI [24] and PID [25] routines have been investigated for RSW control. However, due to inaccurate predictions of weld nugget size, process monitoring and closed-loop control have had limited success in industry [26]. Thus, efforts are still being carried out to improve the robustness of weld nugget size monitoring and control techniques.

The monitoring and control of the small scale resistance spot welding (SSRSW) process is less commonly addressed in the literature than is the large scale resistance spot welding (LSRSW) process although there are some significant differences between the two [27]. Since the workpiece in the small scale process is relatively thin, electrode displacement monitoring requires higher resolution and is much more difficult than for the large scale process. The small scale process is relatively fast, the welding time being typically tens of milliseconds instead of hundreds of milliseconds. The much smaller currents permit the use of higher-bandwidth high frequency inverter or linear power supplies rather than low-to-medium frequency inverters or SCR supplies used in the large scale process. Also the small scale process uses much smaller electrode force.

This work focuses on electrode displacement as a process parameter that is relatively unobtrusive to measure while still offering a substantial amount of information about weld nugget size. In all the published works that use electrode displacement as an approach for monitoring [8,10] or controlling [9,25] the RSW process, maximum electrode displacement measurements were used to calculate weld nugget diameter. However, the informative analysis of Chien and Kannatey-Asibu [11] shows that the maximum electrode displacement/nugget diameter relationship depends on the temperature and thermal strain fields in the welded material in a complex way that is ultimately related to the exact process parameter variations. This indirect relationship between maximum displacement and nugget diameter likely contributes to the failure of displacement-based monitoring systems to achieve more precise predictions of weld nugget size. In the present work, a high-speed video imaging system was employed to directly observe the displacement of the electrodes with relatively high resolution. The nugget size/electrode displacement relationship was studied in detail with a goal to formulating a more accurate relationship between the two.

2 Experimental

A Unitek Miyachi high frequency inverter power supply coupled to a pneumatically-actuated small-scale resistance weld head was used to produce resistance spot welds. The voltage, current, displacement and force change were monitored during the welding cycles using a computer data acquisition system with a sampling rate of 50 kHz per channel. Solid RWMA class 2 electrodes with a tip diameter of 2.38 mm (3/32 inch) were rigidly clamped onto welding head (there was no electrode cooling water) and the welding force was 176 N (40 lb). The material used for the 2-ply lap welds was AISI 302 austenitic stainless steel with a thickness of 0.254 mm (0.01 in.). After welding, the joints were iteratively sectioned, polished and etched to determine the maximum nugget size.

The thin gauge made accurate measurements of electrode displacement impossible with available LVDT sensors. Although an optical sensor provided sufficient resolution, it was found that dynamic flexure of the sensor mounts introduced measurement

Table 1   Welding current waveform parameters

| # | Preheat pulse | | Welding pulse | | Note |
	Current/kA	Duration/ms	Current/kA	Duration/ms	
1	0.2	0.3	1.0	5.0	
2	0.2	0.3	1.0	7.5	
3	0.2	0.3	1.0	10.0	
4	0.2	0.3	1.0	4.0	
5	0.2	0.3	1.0	3.0	No joining
6	0.3	1.5	1.0	5.0	
7	0.3	1.5	0.8	5.0	
8	0.3	1.5	0.6	5.0	No joining
9	0.3	1.5	1.2	5.0	Large expulsion
10	0.3	1.5	1.2	5.0	Small expulsion
11	0.3	1.5	1.1	5.0	
12	0.3	1.5	0.9	5.0	
13	0.3	1.5	0.7	5.0	No joining
14	0.3	1.5	0.5	5.0	No joining
15	0.005	1.0	1.0	4.0	
16	0.1	1.0	1.0	4.0	
17	0.1	1.0	1.0	3.5	
18	0.1	1.0	0.9	4.5	
19	0.1	1.0	1.0	4.5	

errors [28]. A high-speed CCD digital camera was subsequently implemented to more precisely measure electrode displacement during the welding process. The frame rate of the motion analyzer was set to 4500 per second. A long-distance microscope lens, placed 102mm (4 in.) from the weld location, provided images with a vertical resolution of $1.75 \mu m$/pixel. A fiber optic light source was placed behind the electrodes and workpiece to project a shadow image of the electrodes and workpiece into the camera. Spot welding current and weld time were varied according to an experimental matrix to produce a range of weld nugget sizes. The duration and magnitude of the welding current pulse were changed to vary the input power to workpiece to form different

size of nuggets, as shown in Table 1. It is noted that the Unitek-Miyachi welding power supply employs a two-pulse welding technique where the electrode and material interfaces are conditioned by a low current pulse before the higher current welding pulse.

3   Results and Discussion

Two frames of the motion analyzer images, showing results before and after threshold processing, are displayed in Figs. 1(a) and 1(b). Because of the high magnification, only the right edge of the electrodes and part of the workpiece are visible. Electrodes with a higher-than-normal degree of mushrooming were used to allow accurate measurement of the electrode tip positions. This configuration eliminated measurement errors caused by thermal expansion, elastic deflection and/or mechanical displacement of the electrodes and holders.

The position of each electrode tip was calculated by averaging the position of all the pixels along the edge of the mushroom in the thresholded images. Figure 2 shows a typical electrode displacement curve obtained after frame-by-frame processing of the images. As shown in the figure, when the material expanded in welding, both the upper and the lower electrode tips moved, al-
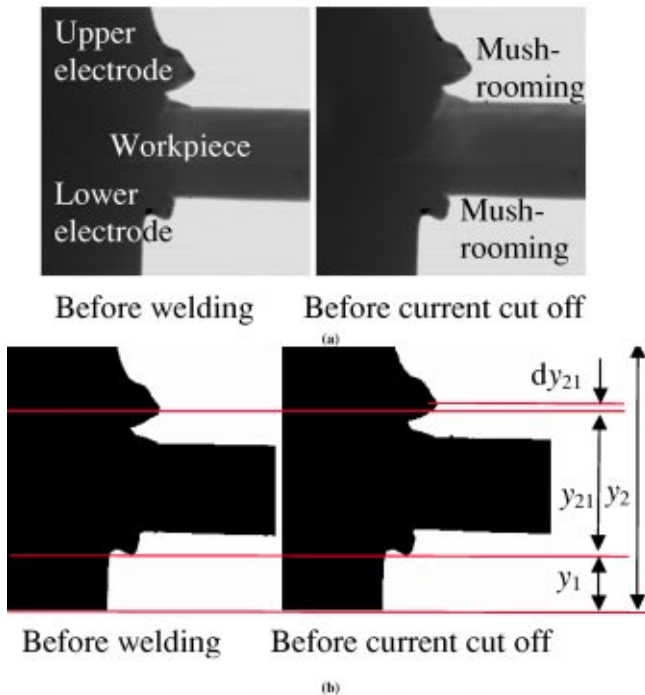

Fig. 1   Obtaining electrode displacement from motion analyzer images (a) original images captured by the analyzer (b) images after threshold processing
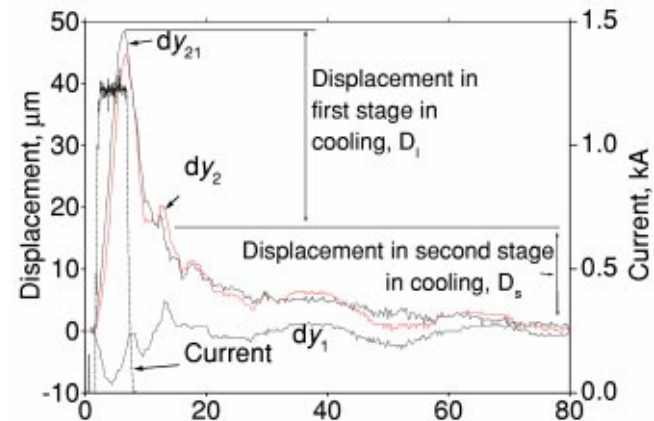

Fig. 2   Displacement of electrodes in welding and the abrupt change of electrode velocity in cooling
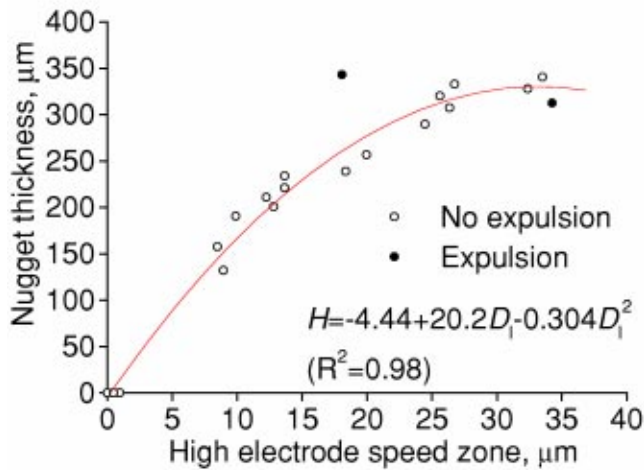
Fig. 3 Relationship of electrode displacement in first stage in cooling to nugget thickness

Fig. 4 Nugget thickness versus maximum electrode displacement

though the lower electrode had much smaller displacement than the upper one. The electrode displacement is defined as the change of the separation between the two tips, termed dy_{21} in the figure. As a practical matter, it should be noted that distortion of larger sheets or the geometry of welded parts might obscure the electrode tips, making this image-based measuring technique difficult to implement in a production setting.

Careful inspection of the electrode displacement curves reveals that the cooling part can typically be divided into two stages as noted in Fig. 2. In the first stage of cooling, the curve has a steeper gradient and the change in dy_{21} during this interval is defined as D_l in the figure. This portion of the electrode displacement curve is believed to correspond to the liquid/solid phase transformation of the weld nugget. If this is true, the second stage (which has a more gradual slope and is labeled D_s in the figure), corresponds to thermal contraction resulting from cooling of the solid phase. This interpretation of the curve is supported by comparison with the specific volume of austenitic stainless steel [29]. The total change in density from liquidus to solidus temperatures is about 0.4 g/cc while the total change from solidus to ambient temperature is about 0.5 g/cc. Thus, if volume change were constrained to occur only in the thickness direction, one would expect the change in electrode displacement during the liquid-solid transition to be comparable to that occurring during the subsequent cooling to ambient temperature. However, the curves in Fig. 2 show that the contraction during the first stage of cooling is about twice that of the second stage. The fact that contraction during the initial cooling phase is larger than expected might be due to the fact that the average liquid temperature is actually higher than liquidus at the end of the welding current pulse. It should also be noted that solid material surrounding the molten nugget will obscure the observed high-speed contraction in thicker materials.

It was also observed that there was a noticeable increase in the slope of the electrode displacement curve shortly after the welding current was initiated. This suggests that the heating part of the displacement curve can also be divided into two stages: the first corresponding to heating of solid material and the second corresponding to liquid/solid transformation as well as further heating of the liquid nugget and the remaining solid material between the electrodes. However, the change in slope observed during heating was generally not as abrupt as that observed during cooling.

The considerations outlined above lead one to predict that the weld nugget thickness (its size in sheet thickness direction) should be better-correlat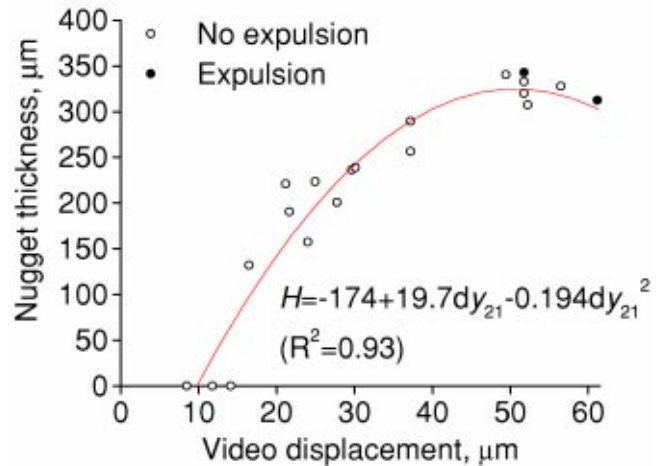ed to electrode displacement than its diameter. To test this hypothesis, the electrode displacement in the first stage of cooling was plotted against the nugget thickness as shown in Fig. 3. This plot shows that this measure of electrode displacement was well-correlated to nugget thickness, even in welds when a small amount of expulsion occurred. In the case welds with a large amount of expulsion, the electrode displacement was less than normal. However, it is reasonable to expect that expulsion would have such an affect. Least squares fitting of a quadratic relation between nugget thickness and electrode displacement resulted in the equation

$$H = 4.44 + 20D_l - 0.304D_l^2 \tag{1}$$

where H is the thickness of nugget and D_l is the electrode displacement as illustrated in Fig. 2. The correlation of the curve fit is excellent, with $R^2 = 0.98$ and a maximum error of 20×10^{-6} m between the curve and the data. This maximum error is only about 6 percent of the largest nugget thickness. Although only weld current and time were varied during the tests, this result indicates that the electrode displacement measured directly at the tips is highly correlated to weld nugget thickness. It is also noted that other parameter variations, such as electrode diameter and sheet thickness, may affect the accuracy of the relationship and their influence merits further study.

It was also found that nugget thickness was closely related to the maximum electrode displacement (Fig. 4). Maximum displacement is of interest since this parameter has been commonly measured by prior researchers. The curve fit plotted in Fig. 4 shows that nugget thickness H is well-predicted by maximum electrode displacement dy_{21} by the relationship

$$H = -174 + 19.7dy_{21} - 0.194dy_{21}^2. \tag{2}$$

However, the data is less well correlated with $R^2 = 0.93$ and maximum error of 60×10^{-6} m (approximately 20 percent of the largest nugget thickness). We also note that the relationship between the high-speed electrode displacement during the second heating stage and the nugget thickness, which is not shown, had a correlation of $R^2 = 0.93$ and a maximum error of about 50×10^{-6} m.

Since spot weld shear strength is more closely related to nugget diameter than nugget thickness, diameter is usually regarded as a
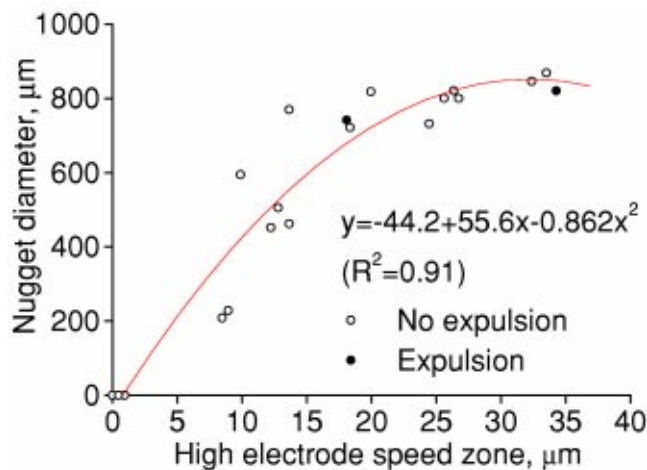
Fig. 5   Nugget diameter versus displacement in first stage in cooling

more important quantity to measure or control. However, these results show that electrode displacement, which is sometimes used for this purpose, is not as closely correlated to nugget diameter as it is to nugget thickness. This is illustrated in Fig. 5, where the correlation of high-speed electrode displacement during the first cooling stage and nugget diameter only has $R^2 = 0.91$ and a maximum error of about 200×10^{-6} m (25 percent of the largest diameter). The total electrode displacement, which is more commonly used in practice, was also more closely correlated to nugget thickness than to nugget diameter. Assuming that it is generally true, this result has important implications for the accuracy of resistance spot welding controls that are based on electrode displacement.

4   Conclusions

1. The relationship between electrode displacement and RSW nugget size was studied using high resolution video camera measurements of the electrode tips.

2. The correlation between the nugget thickness and electrode displacement during the first stage of cooling was best of all correlations that were studied. The average correlation coefficient of a quadratic fit was $R^2 = 0.98$ the maximum error was about 6% of the largest nugget thickness.

3. The maximum electrode displacement, which is usually measured for RSW monitoring and control, was less well correlated to nugget thickness, with $R^2 = 0.93$ and maximum residual error of about 20%.

4. All measures of electrode displacement that were investigated were better correlated to weld nugget thickness than they were weld nugget diameter.

Acknowledgments

References

[1] Ely, K. J., and Zhou, Y., 2001, "Microresistance Spot Welding of Kovar, Steel, and Nickel," Sci. Technol. Weld. Joining, **6**(2), pp. 63–72.

[2] Williams, N. T., 1997, "Use of Voltage Integration for Monitoring and Feedback," *Resistance Welding Control and Monitoring*, TWI, pp. 13–18.

[3] Dickinson, D. W., Franklin, J. E., and Stanya, A., 1980, "Characterization of Spot Welding Behavior by Dynamic Electrical Parameter Monitoring," Weld. J. (Miami, FL, U. S.), **59**(6), pp. 170s–176s.

[4] Patange, S. R., Anjaneyulu, T., and Reddy, G. P., 1985, "Microprocessor-based Resistance Welding Monitor," Weld. J. (Miami, FL, U. S.), **64**(12), pp. 33–38.

[5] Livshits, A. G., 1997, "Universal Quality Assurance Method for Resistance Spot Welding Based on Dynamic Resistance," Weld. J. (Miami, FL, U. S.), **76**(9), pp. 383s–390s.

[6] Gedeon, S. A., Sorensen, C. D., Ulrich, K. T., and Eagar, T. W., 1987, "Measurement of Dynamic Electrical and Mechanical Properties of Resistance Spot Welds," Weld. J. (Miami, FL, U. S.), **66**(12), pp. 378s–385s.

[7] Li, W., Hu, S. J., and Ni, J., 2000, "A Method for On-Line Quality Prediction of Resistance Spot Welding," ASME J. Manuf. Sci. Eng., **122**(3), pp. 511–512.

[8] Waller, D. N., and Knowlson, P. M., 1965, "Electrode Separation Applied to Quality Control in Resistance Welding," Weld. J. (Miami, FL, U. S.), **44**(4), pp. 168s–174s.

[9] Wood, R. T., Bauer, L. W., Bedard, J. F., Bernstein, B. M., Czechowski, J., D'ndrea, M. M., and Hogle, R. A., 1985, "A Closed-loop Control System for Three-phase Resistance Spot Welding," Weld. J. (Miami, FL, U. S.), **64**(12), pp. 26–30.

[10] Taylor, J. L., and Xie, P., 1987, "A New Approach to the Displacement Monitor in Resistance Spot Welding of Mild Steel Sheet," Metal Construction, **19**(2), pp. 72–75.

[11] Chien, C. S., and Kannatey-Asibu, E., Jr., 1998, "Displacement Measurement Using a Fiber Optic Sensor in Resistance Spot Welding," Trends in Welding Research, *Proc. of the 5th Inter. Conf.*, Pine Mountain, Georgia, pp. 622–627.

[12] Beemer, R. D., and Talbot, T. W., 1970, "Analyzer for Nondestructive Process Control of Resistance Welding," Weld. J. (Miami, FL, U. S.), **49**(1), pp. 9s–13s.

[13] Mironov, L. G., Afanasev, L. K., and Zaitsev, V. A., 1979, "Control of the Quality of Welds Directly during Resistance Spot Welding," Welding Production, **26**(2), pp. 40–43.

[14] Heb, J., Kern, T., Kriegl, W., and Schweizer, M., 1998, "Visualization of the Resistance Spot Welding Process in the Production Line," Weld. J. (Miami, FL, U. S.), **77**(12), pp. 495s–502s.

[15] Hirsch, R. B., 1993, "Tip Force Control Equals Spot Weld Quality," Weld. J. (Miami, FL, U. S.), **72**(3), pp. 57–60.

[16] Tang, H., Hou, W., Hu, S. J., and Zhang, H., 2000, "Force Characteristics in Resistance Spot Welding," Weld. J. (Miami, FL, U. S.), **79**(7), pp. 175s–183s.

[17] Mansour, T. M., 1988, "Ultrasonic Inspection of Spot Welds in Thin-gage Steel," Mater. Eval., **46**(4), pp. 650–658.

[18] Beatson, E. V., 1977, "An Introduction to Quality Control Systems in Resistance Welding," Resistance Welding Control and Monitoring, TWI, pp. 2–7.

[19] Satonaka, S., and Matsuyama, K., 2000, "Review on Inspection Techniques for Spot Welds," Welding on the World, **44**(3), pp. 4–10.

[20] Messler, R. W., and Jou, M., 1996 "A Review of Control Systems for Resistance Spot Welding," Sci. Technol. Weld. Joining, **1**(1), pp. 1–9.

[21] Shriver, J., Peng, H., and Hu, S. J., 1999, "Control of Resistance Spot Welding," *Proceedings of the American Control Conference*, San Diego, California, June, pp. 187–191.

[22] Brown, J. D., Rodd, M. G., and Williams, N. T., 1998, "Application of Artificial Intelligence Techniques to Resistance Spot Welding," Ironmaking Steelmaking, **25**(3), pp. 199–204.

[23] Jou, M., Li, C. J., and Messler, R. W., Jr., 1998, "Controlling Resistance Spot Welding Using Neural Network and Fuzzy Logic," Sci. Technol. Weld. Joining, **3**(1), pp. 42–50.

[24] Chang, H. S., Cho, Y. J., Choi, S. G., and Cho, H. S., 1989, "A Proportional-integral Controller for Resistance Spot Welding Using Nugget Expansion," ASME J. Dyn. Syst., Meas., Control, **111**(2), pp. 332–336.

[25] Haefner, K., Carey, B., Bernstein, B., Overton, K., and D'Andrea, M., 1991, "Real-time Adaptive Spot Welding Control," ASME J. Dyn. Syst., Meas., Control, **113**(1), pp. 104–112.

[26] Irving, B., 1996, "The Search Goes on for the Perfect Resistance Welding Control," Weld. J. (Miami, FL, U. S.), **75**(1), pp. 63–68.

[27] Chang, B. H., Li, M. V., and Zhou, Y., 2001, "Comparative Study of Small Scale and 'Large Scale' Resistance Spot Welding," Sci. Technol. Weld. Joining, **6**(5), pp. 273–280.

[28] Farson, D., Chen, J., Ely, K., and Frech, T., 2003, "Monitoring of Expulsion in Small Scale Resistance Spot Welding," Sci. Technol. Weld. Joining, **8**(6), pp. 431–436.

[29] Overfelt, R. A., Taylor, R. E., and Bakhtiyarov, S. I., 2000, "Thermophysical Properties of A356 Aluminum, Class 40 Gray Iron, and CF8M Stainless Steel," AFS Trans., **108**, pp. 369–376.

A New Tool Wear Examination Model by Least Square Method for Shearing Process of Thin Metal Sheet

Zone-Ching Lin

Professor,
Department of Mechanical Engineering, National Taiwan University of Science and Technology, Taipei, Taiwan, R.O.C.
e-mail: zclin@mail.ntust.edu.tw

Dar-Yuan Chang

Assistant Professor,
Department of Mechanical Engineering, De Lin Institute of Technology, Tucheng, Taipei Hsien, Taiwan, R.O.C.
e-mail: dyc@dlit.edu.tw

A new method that accounts for material loss in the normal direction has been developed. Most research applied wear length and wear area to present the status of the tool. Nevertheless, these methods cannot detect the wear in the normal direction of the contact surface between tool and material, and cannot make accurate judgments in precision machining process. In the proposed model, both of the least square lines of the inspected positions and the least square planes of the examined flanks calculating by the wear depth of measuring points are used to infer the relative wear indices, such as flank wear angle, wear depth of punch top face, straightness error, area loss, and volume loss of punch flanks. By using these indices more objective estimations can be acquired than that of wear length and wear area. A series of shearing experiments of thin phosphor bronze sheet are executed to explore the effects of shearing parameters on punch flank wear, and several regressive equations are derived to express the relationships between the wear indices and number of shearing strokes. [DOI: 10.1115/1.1644551]

1 Introduction

In studies of tool machining, the tool condition has always been presented either by wear length and wear area based on the tool images obtained from various microscopes [1–5], or the tip radii of cutting edge [6–7]. Although the wear length and the wear area can provide the information of machining surface, they cannot detect the wear in the normal direction on the contact surface between tool and sheet.

During the high-speed shearing process, punch flank wear varies from the setting of shearing parameters; however, the wear volume affects the punch width directly, and then the punching dimension has also be influenced [3,8]. Consequently, how to measure the punch flank wear in the normal direction becomes a worthy issue to be studied.

Figure 1 shows the illustration of the shearing principle. A number of studies [9–11] explored the influence of the punch sheared angle on the shearing force and the punch-die clearance on the shearing quality [8,12–13]. In addition, many studies were devoted to constructing the simulation models of the sheet shearing process by the finite element method in order to analyze the sheets fracture processes, and then applying the developed model, one

may infer the crack start position, the plastic deformation zone of sheared surface, the influences of punch geometry features on plastic deformation zone, and the final profile of the sheared products [14–16].

In the machining process, tool wear can be regarded as one kind of systematic variation, and usually can be presented as a time series problem [17,18]. Most academic research believed that the flank wear mostly affects the machining quality of the part [4,19–21]. Cheung et al. [19] revealed that the wear land of punch flank was larger than that of punch top face, and the wear of punch cutting edge was greater than that of die block blades in the lower shoe. In Luo's shearing experiments [22], the results showed that the punch wear mainly took place at the punch flank. Hence, this study focused the issue on punch flank wear.

In order to explore the effects of shearing parameters on tool wear, a series of shearing experiments of thin phosphor bronze sheet are executed. The analytical parameters include a number of shearing strokes, punch-die clearance, punch sheared angle, and hardness ratio between the punch and the sheet. The results of this study provide valid references for thin metal shearing process of progressive die.

2 Experimental Scheme

Tables 1 and 2 list the parameters plan of the experiments and the chemical ingredients of the materials of punches and sheets. The experimental strip designed to simulate the dam-bar cutting process in IC leadframe fabrication is illustrated in Fig. 2. The area highlighted by monocline lines in the middle drawing is the simulated lead, and the blanks are the materials removed during the process. Material between the two rectangles is called dambar, and the two leads at the right are the leads finishing the shearing process. Detailed dimensions of the simulated lead show in the left drawing, and the cross grids in the right drawing pinpoint the position of the dam-bar cutting punch investigated.

Figure 3 is the photograph of experimental progressive die. Five machining stations are designed to complete the whole process. *Punch-5* is the dam-bar cutting punch investigated in this study, and the removed area by the dam-bar cutting punch is the product of dam-bar width (WD) and punch width (PW). The picture at the right bottom is the progressive die in processing in which the strip is progressed from the left hand to the right hand. The thickness of metal sheet is 0.254 mm. he frequency of punch stokes is set as $450\,SPM$, and the punch stroke is 4 mm; therefore, the shearing speed is 60 mm/sec. Experiments, were followed by inspections and analyses.

3 Punch Wear Models

This study proposes a tool wear examination model based on the least square method for the progressive shearing die. First, measure the height of the measuring points at the three examined positions which sit at shear center and near the shear boundaries. The least square lines of the three examined positions and the least square plane of the tool flank can be calculated based on the height data measured. Next, calculate the wear indices of the examined positions including flank wear angle, flank wear length, area loss, straightness error, and wear depth of the punch top based on the least square lines calculated. Afterwards, the gradient, normal vector, and volume loss of the punch flank were reckoned, too. Final, the tool status can be exactly determined by means of these indices. The followings are the descriptions of the analytical procedures.

3.1 Wear Calculation Based on Least Square Line. Assume that the least square line calculated from the height of measuring points is $y=ax+b$. Based on the definition of least square error, the sum of square error, δ, of the measuring points and the corresponding positions of the least square line is
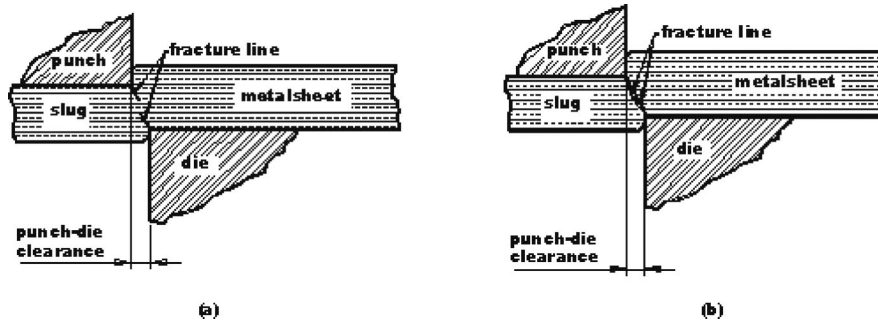
Fig. 1   Illustration of metal shearing principle

$$\delta = \sum_{i=1}^{n} (y_i - y)^2 \qquad (1)$$

Substitute $y = ax_i + b$ into Eq. (1), the coefficients of a and b can be derived, where a and b are the slope and the intercept of the least square line, respectively. Two parallel lines passing the highest and the lowest measuring points are made based on the least square line. The deviation between the two parallel lines in vertical direction is defined as *straightness error*, expressed as

$$Err_{straightness} = \delta_{upper} + \delta_{lower} \qquad (2)$$

where δ_{upper} and δ_{lower} are the distance from the least square line to the two parallel lines, respectively.

Figure 4 shows the examined punch model. The calculation procedures are described as follows:

(1) Calculate the least square line, $z = ay + b$, of the examined position by the height of the measuring points. In this model, intercept b is negative.

(2) Calculate the punch wear angle, θ_W, by slope a, expressed as

$$\theta_W = \tan^{-1}(a) \qquad (3)$$

(3) Calculate the wear depth of punch top, z_{TOP}, by a, b, and the coordinate of x-axis, expressed as

$$z_{TOP} = z_{TOP}(x) = a \cdot x \cdot \sin(\theta_T) + b \qquad (4)$$

Table 1   Scheme of thin metal sheet shearing experiments

Exp. No	Punch material	Punch-die clearance (mm)	Punch sheared angle (degrees)	Metal sheet	Number of shearing stroke (thousand)	Hardness ratio	Explosion factors
1a	ASP60	0.076	0	C5191-RH	**10**	4.75	Shearing stroke
1b	ASP60	0.076	0	C5191-RH	**20**	(940/198)	
1c	ASP60	0.076	0	C5191-RH	**25**		
1d	ASP60	0.076	0	C5191-RH	**30**		
1e	ASP60	0.076	0	C5191-RH	**40**		
1f	ASP60	0.076	0	C5191-RH	**50**		
1g	ASP60	0.076	0	C5191-RH	**60**		
1h	ASP60	0.076	0	C5191-RH	**70**		
2a	SKH9	**0.078**	0	C5191-RH	15	1.39	Punch-die clearance
2b	SKH9	**0.060**	0	C5191-RH	15	(275/198)	
2c	SKH9	**0.047**	0	C5191-RH	15		
2d	ASP60	**0.077**	0	C5191-RH	15	4.75	
2e	ASP60	**0.060**	0	C5191-RH	15	(940/198)	
2f	ASP60	**0.051**	0	C5191-RH	15		
3a	ASP60	0.039	**0.5**	C5210	30	4.18	Punch sheared angle
3b	ASP60	0.037	**10**	C5210	30	(940/225)	
3c	ASP60	0.040	**20**	C5210	30		
3d	WC	0.040	**0.5**	C5210	30	5.88	
3e	WC	0.040	**10**	C5210	30	(1323/225)	
3f	WC	0.041	**20**	C5210	30		

Table 2   Alloy ingredients and mechanical properties of punches and sheets (%)

Components	C	Cr	Mo	W	V	Co	Hardness
ASP60	2.3	4.2	7.0	6.5	6.5	10.5	66–68 H_RC (940 Hv)
SKH9	0.87	4.2	5.0	6.4	1.9	—	261 HB (275 Hv)
WC			85% Tungsten Carbide, 15% cobalt				88.5 H_RA (1323 Hv)

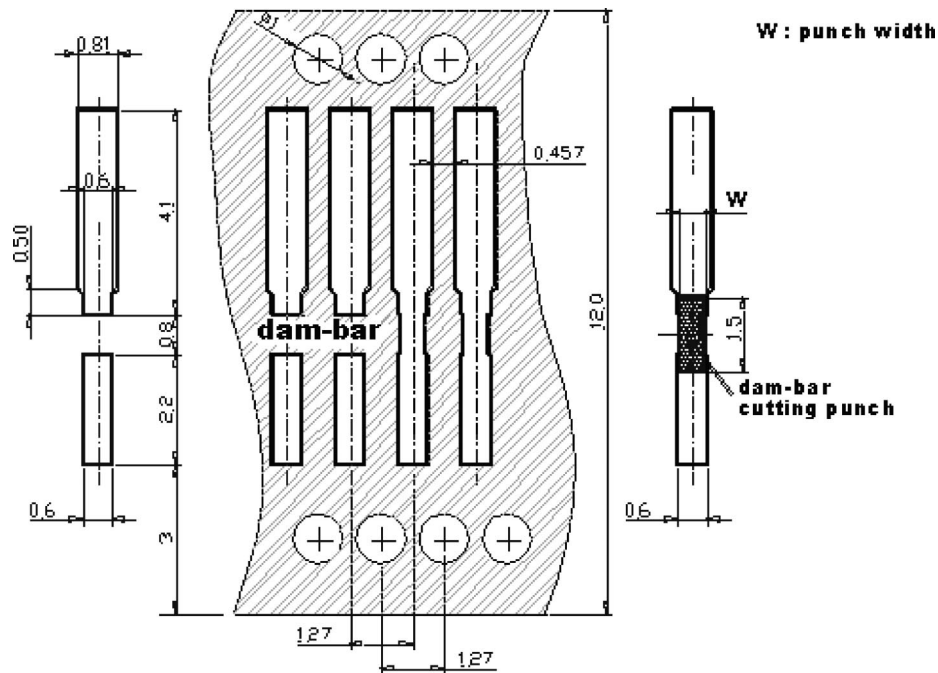| Components	Cu	Sn	P	Zn	Pb	Fe	Hardness (Hv)	Yield strength (kgf/mm²)	Tensile strength (kgf/mm²)
C5191R-H	93.7530	6.1050	0.1108	0.0144	0.0030	0.0088	196–198	55.2	61.3
C5210	91.895	7.9584	0.1065	0.0157	0.0059	0.0107	223–225	62.5	70.0

Fig. 2 Schematic diagram of experimental strip

where θ_T is the punch sheared angle. When a flat punch is used, the wear depth of punch top is equal to intercept b.

(4) Calculate the flank wear length, WL, by a, b, and θ_T.

$$WL = WL(x) = b/a - x \cdot \sin(\theta_T) \qquad (5)$$

(5) According to z_{TOP} and WL, calculate the area loss, WA_{FLANK}, of the examined position.

$$WA_{FLANK} = \frac{1}{2} \cdot z_{TOP} \cdot WL = \frac{b^2 - (a \cdot x \cdot \sin \theta_T)^2}{2a} \qquad (6)$$

(6) Final, evaluate the wear condition of the punch flank based on the indices of z_{TOP}, θ_W, WA_{FLANK}, WL, and $Err_{straightness}$. More detailed descriptions are presented in Sec. 4.
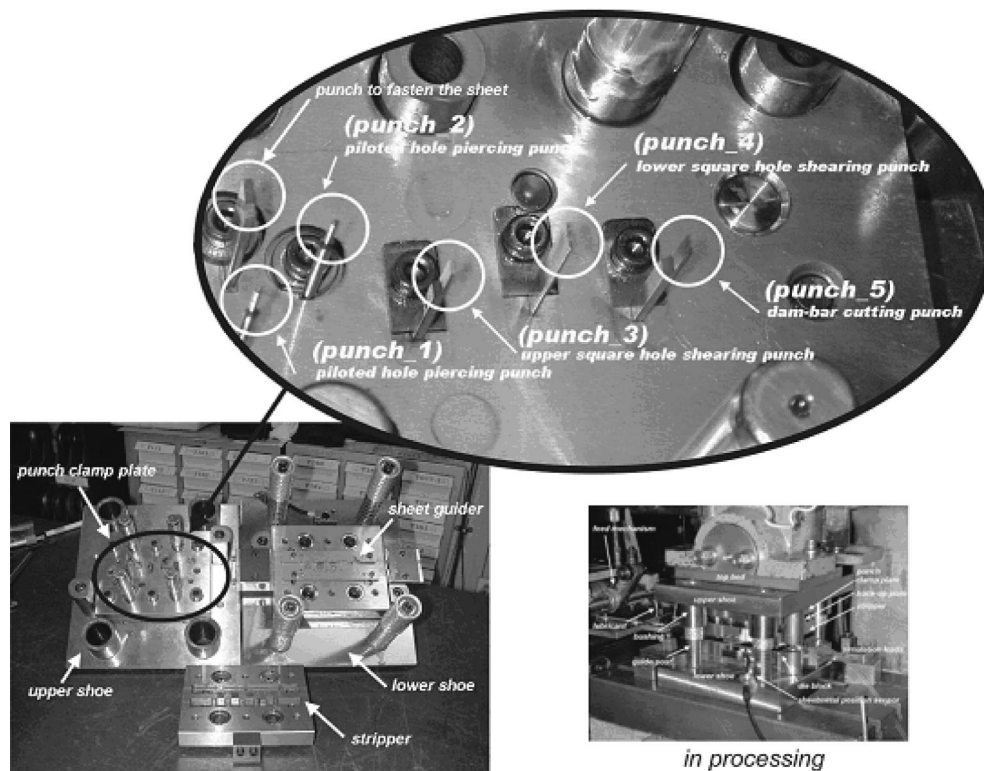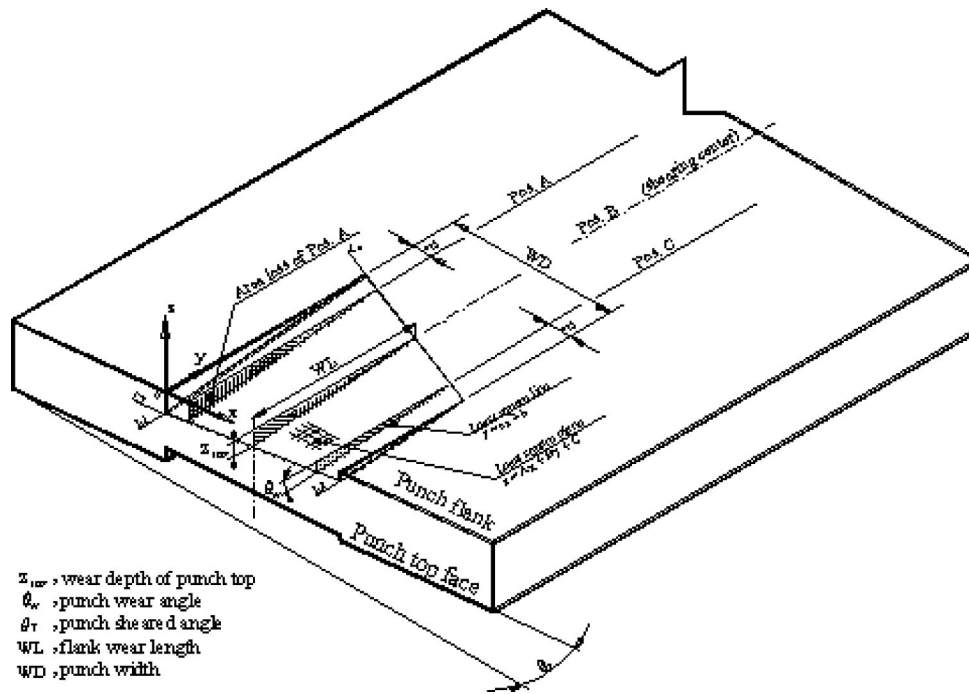

Fig. 3 Photographs of experimental progressive die

Fig. 4 Punch wear examination model

Z_{top} , wear depth of punch top
θ_w , punch wear angle
θ_T , punch sheared angle
WL , flank wear length
WD , punch width

3.2 Punch Flank Volume Loss. The wear loss of the whole punch can be evaluated by the least square plane of the flank. Assume that the least square plane of the punch flank calculated by the measuring points is $z = Ax + By + C$. Then, the deviation between the measuring point, (X_i, Y_i, Z_i), and the corresponding position on least square plane in z-axis is written as:

$$d_i = Z_i - (Ax_i + By_i + C) \tag{7}$$

The sum of square error between the measuring points and the corresponding points on least square plane is calculated by

$$\delta = \sum_{i=1}^{n} (d_i)^2 \tag{8}$$

According to the definition of the least square method, the coefficients of A, B, and C can be derived. The intercepts of the three axes are $l = -C/A$, $m = -C/B$, $n = C$, respectively. As the punch model shows in Fig. 4, intercept m of y-axis is greater than zero and the intercept n of z-axis is less than zero. However, the intercept l of x-axis is decided by the normal vector of least square plane.

The volume loss for a flat punch, $\theta_T = 0$, can be calculated by the following formula.

$$V_{L\_FLAT} = \int \int_V \int dV = \int_0^{WD} \int_0^{-(AX+C)/B} \int_{Ax+By+C}^{0} dz\,dy\,dx$$

$$= \frac{WD}{6B}(A^2 \cdot WD^2 + 3A \cdot C \cdot WD + 3C^2) \tag{9}$$

As for a punch with sheared angle θ_T, the volume loss is smaller than that of a flat one due to its geometric shape. The volume difference, V_1, is calculated by

$$V_1 = \int \int_v \int dv = \int_0^{WD} \int_0^{\tan \theta_T \cdot x} \int_{Ax+By+C}^{0} dz\,dy\,dx$$

$$= \frac{-\tan \theta_T \cdot WD^2}{6}[(2A + B\tan \theta_T) \cdot WD + 3C] \tag{10}$$

Consequently, the volume loss of a punch with sheared angle, V_{L_ANG}, is

$$V_{L\_ANG} = V_{L\_FLAT} - V_1 \tag{11}$$

3.3 Height Measurement of Punch Flank. Figure 5 shows the measuring points of punch flank in this model. The punch wear width of the shearing experiments is 0.8 mm, and the actual sliding distance between the flank and the sheet is 1.75 mm during the process. Three inspected lines are set based on the examined positions. Two of them set as 0.05 mm apart from the left and the right shearing boundaries and the other one sets at shear center. The height measurements carried out at seven positions along the y-axis of each inspected line, as the dot marks shown in Fig. 5. Therefore, each flank has 21 sets of measurement data, and the area marked with two bold dot lines is the flank wear region.

The measurement process uses an optical projector with a 50X magnified lens. The examined punches are placed on the platform, and the measuring position is controlled by the displacement mechanism of the projector with 1 μm precision. The wear depth of each measuring point can be read from an electronic comparison apparatus with resolution of 0.1 μm.

4 Experimental Results and Discussions

This study executed a series of high speed shearing experiments of thin phosphor bronze sheet to explore the effects of the parameters including the number of shearing strokes, punch-die clearance, punch sheared angle, and hardness ratio of punch and sheet, on the punch wear.
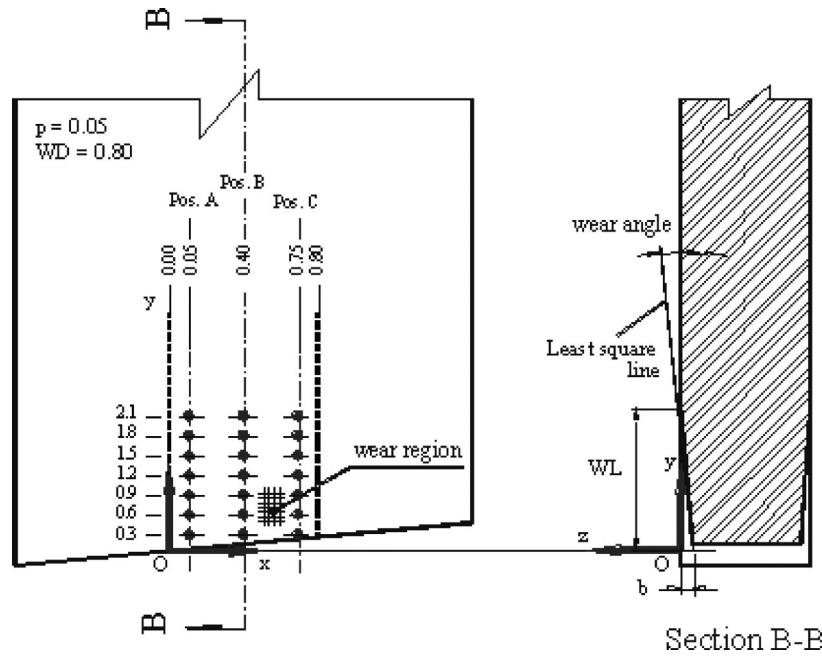
Fig. 5 Schematic diagram of measuring points on punch flank

4.1 Effects of Number of Shearing Strokes on Punch Wear
The first case executed eight shearing experiments with different strokes, as the experiments schemed in Sec. 2. There were a total of 16 flanks to be measured of the 8 experimental punches. Each flank carried out the height measurements at the three inspected lines of 21 measuring points. Because the two inspected lines near the shearing boundaries were easily affected by other shearing factors, this study implemented the wear analysis by the data of shear center (*Pos. B*).

Table 3 lists all the wear indices calculated of the punches in *Exp-1*. Figure 6 shows the relationships between the number of shearing strokes and the wear indices including wear depth of punch top, flank wear angle, flank wear length, and flank area loss of the examined position. From the viewpoint of materials, the index of area loss is the most objective one to display the wear condition among the four, as shown in Fig. 6(d). In this case, the punch was in the run-in stage before 25,000 strokes, and the strokes of 25,000–50,000 belonged to the stable growing-up stage, but after 50,000 the punch was rapidly deteriorated.

Figures 6(a)–(b) show the relationships between sharing strokes and both the wear depth of punch top and flank wear angle, respectively. We found that the two curves are very similar to the one of flank area loss (Fig. 6(d)); therefore, both indices can also be used to examine the punch wear. Nevertheless, the index of flank wear length used in most tool wear examinations

cannot obtain a consistent relationship with the index of flank area loss, as shown in Fig. 6(c). The main reason is that the wear length only provided the 1D information, i.e. *y-axis*; it cannot reckon the wear depth on punch flank along the *z-axis*, which affects the shearing quality significantly. Therefore, the wear length of flank is not suitable to wear examination in high-speed sheet shearing process.

From the above discussions, we conclude that three indices of wear depth of punch top, punch sheared angle, and area losses are proper to be used in the examination of punch flank wear. The curve fitting works are conducted by five analysis modes, such as linear mode, exponential function, 2-orders polynomial, 3-orders polynomial, and 4-orders polynomial. The fitting equations of the number of shearing strokes and above three indices are derived, in which the mean square error of 3-orders polynomial is the least among the five, as expressed in Eqs. (12)–(14). These equations can be used in punch wear estimation for the thin sheet shearing process.

Wear depth of punch top face, z_{TOP}

$$Z_{TOP} = 1.031885817 + 0.1282985252 \cdot x - 3.099 \times 10^{-3} \cdot x^2$$
$$+ 3.657 \times 10^{-5} \cdot x^3 \tag{12}$$

Flank wear angle, θ_W

Table 3 Wear indices of shear center of *Exp-1*

Exp.-	Number of strokes (thousand)	Wear depth (μm)	Flank wear angle (degree)	Flank wear length (μm)	Area loss (μm^2)	Straightness error (μm)	Sum of WA_{FLANK} (μm)^2	Sum of V_{L_FLAT} (μm)^3
1a	10	1.89285	0.04870	2252.3500	2108.92728	0.46670	4268403	15960.46
1b	20	2.80715	0.07448	2170.9969	3034.44385	0.79470	5119472	19187.84
1c	25	3.20000	0.09167	1962.9004	3210.17420	0.86843	6027867	22689.16
1d	30	2.95000	0.07734	2246.0278	3243.13798	0.74767	6219055	22634.50
1e	40	3.32140	0.08021	2349.9778	3943.86143	1.49407	6946871	26057.90
1f	50	3.80000	0.09167	2369.7490	4518.12485	0.93753	7515629	28032.66
1g	60	6.22860	0.15470	2300.3795	7184.57645	1.09230	9439480	35109.10
1h	70	7.09285	0.18048	2518.0182	8074.48248	0.76313	11264258	42254.54

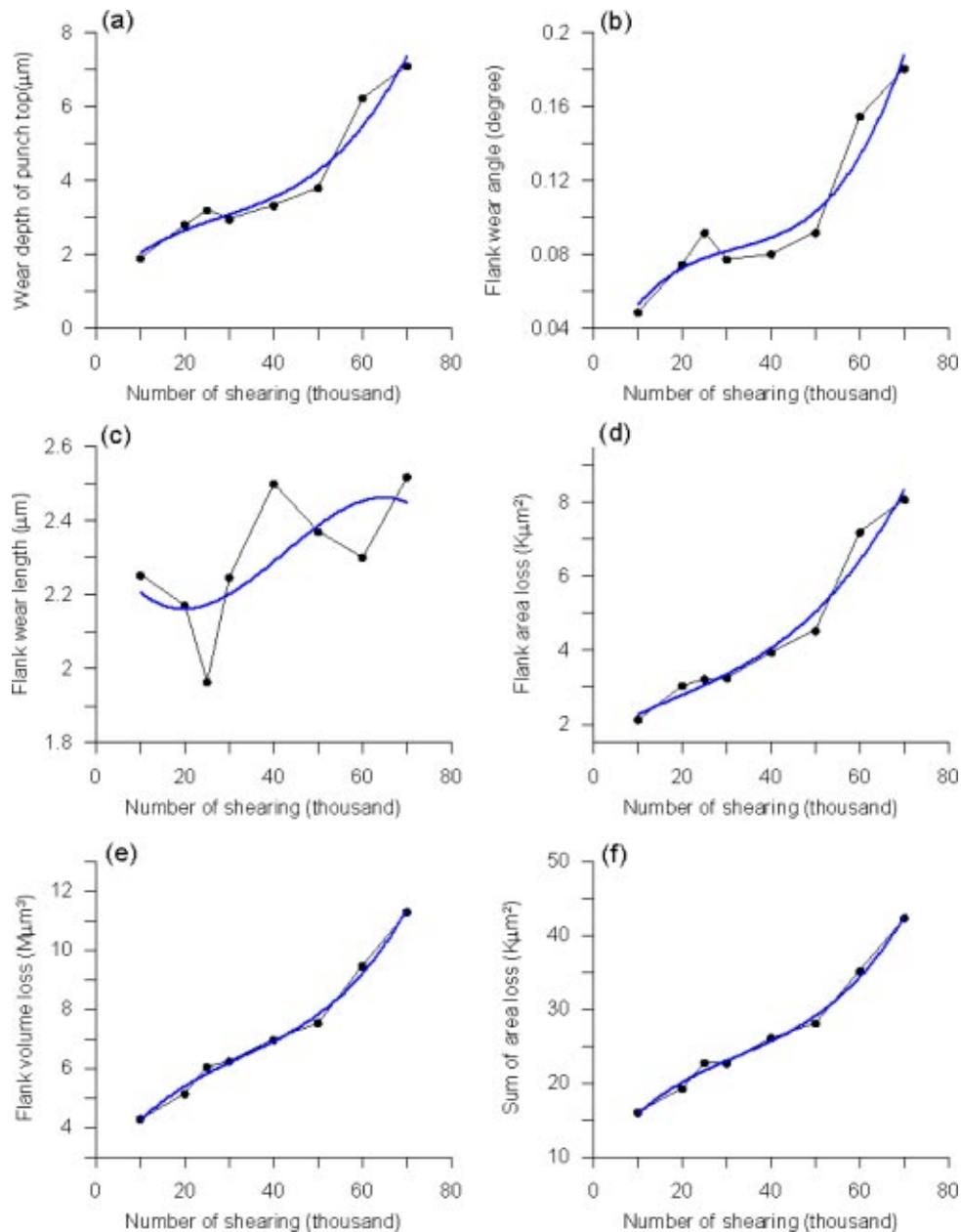PS: Data in table are the index average of two flanks.

Fig. 6 Relationship charts between number of shearing strokes and the related indices of Exp.-1

$$\theta_W = 0.01310662364 + 0.005246138713 \cdot x - 1.431 \times 10^{-4} \cdot x^2$$
$$+ 1.484 \times 10^{-6} \cdot x^3 \qquad (13)$$

Area loss of punch flank, WA_{FLANK}

$$WA_{FLANK} = 1.6457945 + 0.06978977675 \cdot x - 1.045 \times 10^{-3} \cdot x^2$$
$$+ 2.0202 \times 10^{-5} \cdot x^3 \qquad (14)$$

where x is the number of shearing strokes in thousands.

In this case, the straightness errors listed in the seventh column of Table 3 have a similar result to the wear length. They cannot accurately be used in the examination of punch wear. However, the smaller the straightness error, the better the surface condition of the examined position; that is, it approaches to a straight line. Thus, the wear indices inferred by the proposed model provide a higher credibility. A more detailed discussion is presented in Sec. 4-2.

The examined results of volume loss are listed in the last two columns of Table 3, in which *Sum of WA_{FLANK}* is the summation of wear area of the three examined positions and V_{L_FLAT} is the volume loss of the flank calculated by the least square plane. Both terms magnify as the shearing strokes increase. The relationship charts are shown as Figs. 6(*e*) and 6(*f*). By the same way, the fitting error of 3-orders polynomial is the smallest, expressed as Eqs. (15)–(16).

Sum of area loss of the three inspected lines, *sum of WA_{FLANK}*

$$sum \ of \ WA_{FLANK} = 9.278524009 + 0.8080463592 \cdot x - 1.694$$
$$\times 10^{-2} \cdot x^2 + 1.739 \times 10^{-4} \cdot x^3 \qquad (15)$$

Volume loss of punch flank, V_{L_FLAT}

$$V_{L\_FLAT} = 2.45017783 + 0.2181664937 \cdot x - 4.509 \times 10^{-3} \cdot x^2$$
$$+ 4.579 \times 10^{-5} \cdot x^3 \qquad (16)$$

Table 4   Area loss and straightness error of *Exp-2 and Exp-3*

Exp-	Pos.	Punch-die clearance (0.01%t)	Area loss (μm^2)	Straightness error (μm)	Exp-	Pos.	Punch sheared angle	Area loss (μm^2)	Straightness error (μm)
2a	A	15.35	**3003.9741**	**0.7768**	3a		0.5°	15735.3157	2.8357
2b		11.81	7183.2343	1.3518	3b	A	10°	11739.7553	2.0946
2c		9.25	8601.0174	1.5482	3c		20°	**2804.1021**	**0.5482**
2a	B	15.35	**3184.2163**	**1.2322**	3a		0.5°	16509.9399	3.2690
2b		11.81	8559.7611	1.5929	3b	B	10°	12756.3796	2.2786
2c		9.25	10739.2616	1.9643	3c		20°	**4991.8316**	**1.8250**
2a	C	15.35	**1974.7557**	**0.4893**	3a		0.5°	16197.3949	3.0161
2b		11.81	7966.2200	1.1893	3b	C	10°	11824.1620	2.2768
2c		9.25	8748.8434	1.7465	3c		20°	**3597.9468**	**0.9857**
2d	A	15.15	**2733.1086**	**0.6214**	3d		0.5°	8761.1253	1.5273
2e		11.81	3337.1440	0.7214	3e	A	10°	**3516.6885**	**0.7179**
2f		10.03	6550.9157	1.3232	3f		20°	7644.6229	1.7393
2d	B	15.15	**2414.2921**	**0.6572**	3d		0.5°	9220.4857	1.6518
2e		11.81	3441.6344	0.7429	3e	B	10°	**4864.4514**	**0.9018**
2f		10.03	7354.3859	1.3929	3f		20°	9682.1607	1.8572
2d	C	15.15	**2108.8387**	**0.5929**	3d		0.5°	9021.3195	1.6393
2e		11.81	4100.5137	0.7518	3e	C	10°	**3836.7281**	**0.9214**
2f		10.03	7044.8924	1.2179	3f		20°	8058.4152	1.5572

Average of straightness error (μm)	Exp-2a	Exp-2b	Exp-2c	Exp-2d	Exp-2e	Exp-2f
	0.8327	1.3780	1.7530	0.6238	0.7387	1.3113
Sum of area loss (μm^2)	Exp-3a	Exp-3b	Exp-3c	Exp-3d	Exp-3e	Exp-3f
	48.442	36.320	11.394	27.003	12.218	25.385

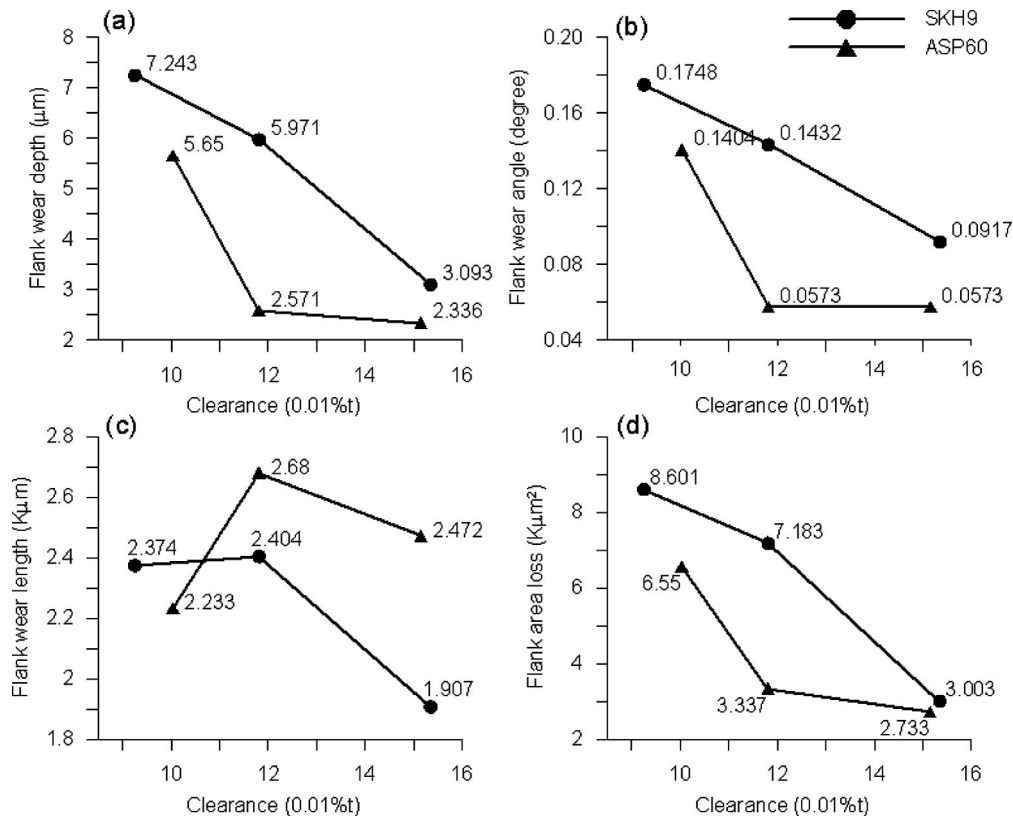PS: Data in table are the average of indices of the two flanks.

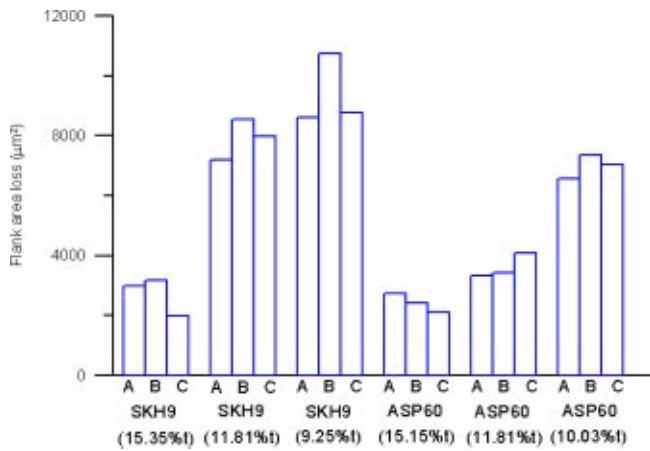Fig. 7   Relationship charts between punch-die clearance and the related indices at *Pos.A* of *Exp.-2*

Fig. 8 Histogram of area loss of *Exp.-2*

As to the flank wear length, as Fig. 6(c) shows, the eight experimental data are far from the fitting curve, and the mean square error is greater than that of the five wear indices. It is obvious that wear indices proposed herein can provide an accurate judgment than the flank wear length.

4.2 Effects of Punch-Die Clearance on Punch Wear. Six experiments programmed by three kinds of punch-die clearances are listed in Table 1. According to the actual widths of shearing punch and punch slot of die block in lower shoe, the clearances was set as $15.35\%\,t$, $11.81\%\,t$ and $9.25\%\,t$ in *Exp-2a–Exp-2c* using *SKH9* punch and that in *Exp-2d–Exp-2f* were $15.15\%\,t$, $11.81\%\,t$ and $10.03\%\,t$ of ASP60 punch respectively, where t is the thickness of metal sheet.

After 15,000 shearing strokes, the area loss and the straightness error of the inspected lines are listed in Table 4, and the relationship charts of the wear indices to various punch-die clearance of the examined position near the left boundary (*Pos. A*, $x=p$) are shown in Fig. 7. Several findings are observed as follows:

(1) From Fig. 7(d), the relationship between area loss and punch-die clearance is in inverse proportion; that is, the area loss of flank extend as the contraction of punch-die clearance. In addition, all the area loss of *SKH9* punches are larger than that of *ASP60* punches for three different clearances.

(2) However, under a larger punch-die clearance such as $15\%\,t$, the area loss of the two kinds of punches is rather close, and the same phenomenon happens in the other two examined positions.

That is to say, when the punch-die clearance extends to $15\%\,t$, flank wear improvement by the hardness ratio of punch and sheet is not obvious.

(3) The analytical results of the wear depth of punch top and the flank wear angle are similar to Sec. 4.1; both are to be used in the wear examination of punch flank, as shown in Figs. 7(a)–7(b). Nevertheless, the relationship between flank wear length and punch-die clearance still has a big difference from the area loss (Fig. 7(c)).

(4) The straightness error can be used to evaluate the surface condition near the inspected position. The last second row of Table 4 lists the average straightness error of the examined positions of *Exp.-2*. The smaller the clearance, *Exp-2c and Exp-2f*, the larger the straightness error, since a more violent friction takes place between the punch and the sheet.

In order to illustrate the area loss of the three examined positions, Fig. 8 shows the histogram of the area loss of *Exp-2*. The bar of shear center, *Pos. B*, is the highest in the three *SKH9* experiments; that is, the maximum flank wear happens at the shear center.

Figure 9 shows the photograph of the sheared surface in *Exp-2d*. When the process enters the tear fracture stage, the plastic deformation is terminated. From the image, the height of tear fracture surface at shear center is greater than that of the boundaries. From the concept of shearing time, the time of the plastic deformation at shear center is the shortest among the three; therefore, the friction effects that materials sustained during the period time is the maximum. In other words, the most violent friction takes place at the shear center. Consequently, the area loss examination model proposed in this study can be verified by the inspection of sheared surface. All six of sheared surfaces in *Exp-2* have the same situation.

As to the *ASP60* experiments, *Exp-2d–Exp-2f*, the area losses are lower than that of *SKH9* experiments, *Exp-2a–Exp-2c* as shown in Fig. 8, but the difference among the three positions is not very distinct. The comparison experiments of the *ASP60* punch and the tungsten steel punch are conducted in next section.

4.3 Effects of Punch Sheared Angle on Punch Wear. In this section, six experiments of *C5210* sheet shearing by *ASP60* punch and tungsten steel punch are executed to explore the effects of the punch sheared angle on punch wear. The number of shearing strokes is increased to 30,000 cycles and the shearing speed is set as 40 mm/sec. The analytical results are listed in the right part of Table 4.

From the data of *Exp-3a–Exp-3c*, which using the *ASP60* punches with a hardness ratio of 4.18, the following results are obtained:
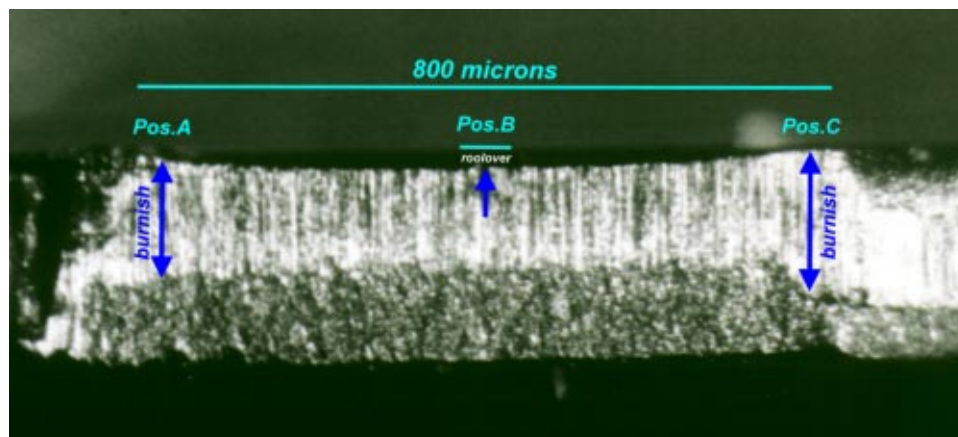

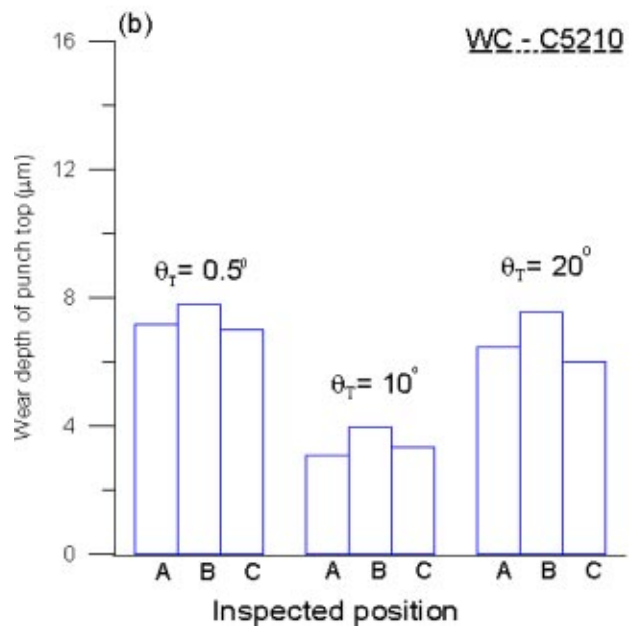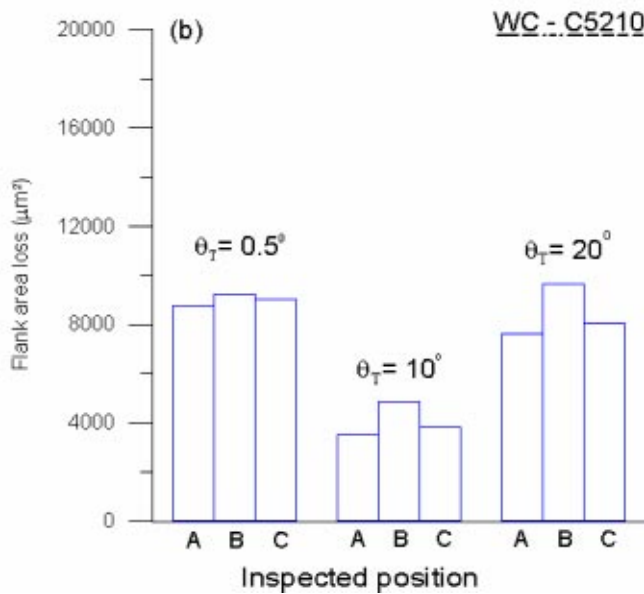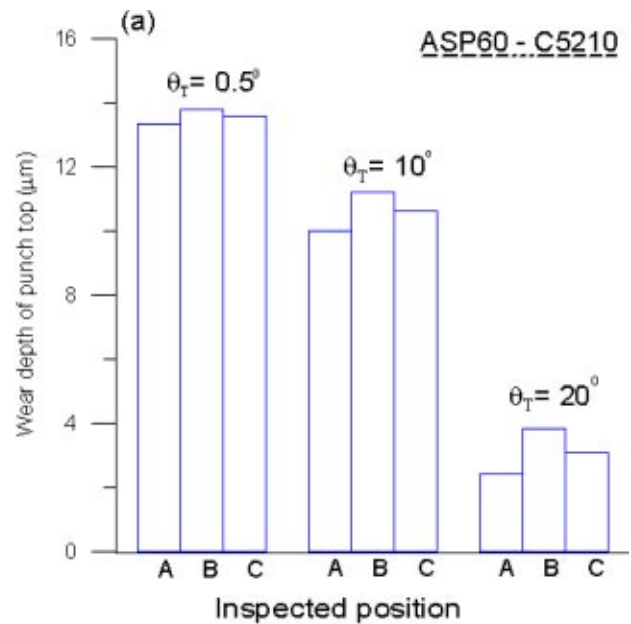**Fig. 9 Photograph of sheared surface punched by *ASP60* punch of *Exp.-2d***
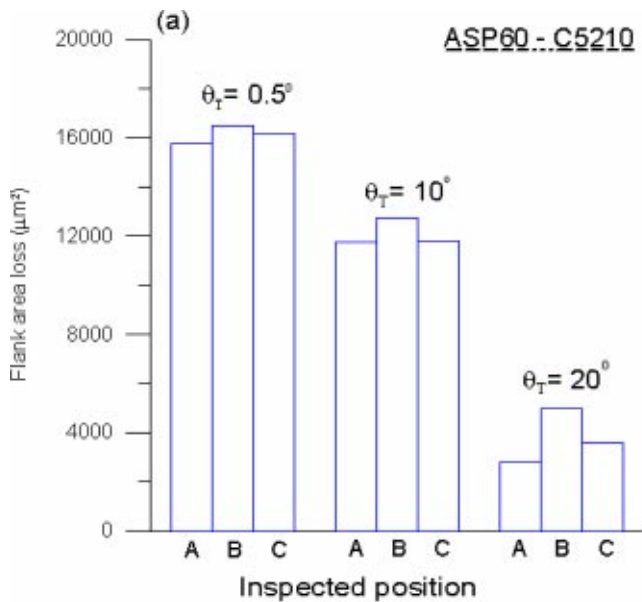
Fig. 10   Histogram of flank area loss of *Exp.-3*

Fig. 11   Histogram of wear depth of punch top of *Exp.-3*

(1) The design of punch sheared angle is contributed to the decrease of punch wear. In this case, area loss of *Exp-3c* with sheared angle of 20° is only one third of that of 30 minutes, as Fig. 10(*a*) shows. Moreover, the scale of wear depth of punch top is merely about 1:4 (9.352:40.76), as shown in Fig. 11(*a*).

(2) From Fig. 10(*a*), we can find that the area loss of the shear center is greater than the others near to the boundaries. Owing to the design of the sheared angle, the area loss of the right inspected line, *Pos. C*, which spends a shorter time in mutual action between the punch flank and materials, is larger than that of the left one, *Pos. A*.

As to the tungsten steel punch, *Exp-3d–Exp-3f*, with a higher hardness ratio of 5.88, since the accomplished shearing strokes are low, the punches still situate in the run-in stage. The analytical results are not similar to the *ASP60* punches providing the regular variation. But, several observations are observed:

(1) The last two columns with shaded marks in Table 4 are the ones with the smallest area loss in *Exp.-3*, and their straightness error also is the smallest in the three examined positions. In other words, both indices of area loss and the straightness error are consistent. Therefore, even in the unstable run-in stage, the straightness error can be regarded as an index for punch wear examination.

(2) The area loss of shear center is the greatest among the three examined positions, as Fig. 10(*b*) shows. The next is the right boundary, *Pos. C*, with the most shortly time of shearing action. This result is the same with that of the *ASP60* punch (Fig. 10(*a*)).

(3) The punch with the sheared angle of 10° has the minimum area loss among the three, and the wear depth of punch top also has the same results, as shown in Figs. 10(*b*) and 11(*b*).

The last row in Table 4 is the sum of area loss of the six punches in *Exp. 3*. When the sheared angle is less than 10°, two kinds of punches have the same tendency to slow down the flank wear. Nevertheless, as the sheared angle increased to 20°, the tungsten steel punch with a higher hardness ratio could not obtain the expected effect of lowering punch wear.

5 Conclusions

This study successfully proposes a tool wear examination model by using least the square method to judge the punch flank wear for thin metal sheet shearing process. It can improve the drawback of lacking the information on the punch wear depth in the presentations of wear length and wear area. A total of twenty experiments of thin metal sheet shearing were conducted, to explore the effects of shearing parameters, such as the number of shearing strokes, punch-die clearance, and punch sheared angle, on punch flank wear. The analytical results show that the proposed wear indices, such as wear depth of punch top, flank wear angle, and flank area loss, could derive more objective expressions than that of wear length. In addition, the indices of straightness error of inspected line and the volume loss of the flank are also accurate in presenting the punch situation.

Punch flank wears increase as the increment of shearing strokes. Five fitting curves regressed by 3-orders polynomial are derived to present the relationships between the number of shearing strokes and the related wear indices. These equations can be provided as valid references in the metal shearing process of thin phosphor bronze sheet.

Acknowledgment

References

[1] Dong, X., Li, S., and Venuvinod, P. K., 2000, "Hybrid Learning for Tool Wear Monitoring," International Journal of Advanced Manufacturing Technology, **16**, pp. 303–307.
[2] Klocke, F., and Raedt, H. W., 2001, "Formulation and Testing of Optimised Coating Properties With Regard to Tribological Performance in Cold Forging and Fine Blanking Applications," Int. J. Refract. Met. Hard Mater., **19**, pp. 495–505.
[3] Cheung, C. F., Lee, W. B., and Chiu, W. M., 2001, "Effect of Tool Wear on Force and Quality in Dam-Bar Cutting of Integrated Circuit Package," ASME J. Electron. Packag., **123**, pp. 34–41.
[4] Braghini, A. B., Jr., and Coelho, R. T., 2001, "An Investigation of the Wear Mechanisms of Polycrystalline Cubic Boron Nitride (PCBN) Tools When End Milling Hardened Steels at Low/Medium Cutting Speeds," International Journal of Advanced Manufacturing Technology, **17**, pp. 244–257.
[5] Kassim, A. A., Mannan, M. A., and Jing, M., 2000, "Machine Tool Condition Monitoring Using Workpiece Surface Texture Analysis," Journal of Machine Vision and Applications, **11**, pp. 257–263.
[6] Hambli, R., and Potiron, A., 2000, "Finite Element Modeling of Sheet-Metal Blanking Operations With Experimental Verification," J. Mater. Process. Technol., **102**, pp. 257–265.
[7] Hambli, R., 2001, "Blanking Tool Wear Modeling Using the Finite Element Method," Int. J. Mach. Tools Manuf., **41**, pp. 1815–1829.
[8] Faura, F., Sebastian, M. A., and Zamora, R., 2001, "A Decision Support System for Sheet Metal Blanking Process Parameters Selection," J. Mater. Process. Technol., **118**, pp. 371–376.
[9] Cheung, C. F., Lee, W. B., and Chiu, W. M., 2000, "An Investigation of Tool Wear in the Dam-Bar Cutting of Integrated Circuit Packages," Wear, **237**, pp. 274–282.
[10] Luo, S. Y., 1999, "Effect of the Geometry and the Surface Treatment of Punching Tools on the Tool Life and Wear Conditions in the Piercing of Thick Steel Plate," J. Mater. Process. Technol., **88**, pp. 122–133.
[11] Singh, U. P., Streppel, A. H., and Kals, H. J. J., 1992, "Design Study of the Geometry of a Punching/Blanking Tool," J. Mater. Process. Technol., **33**, pp. 331–345.
[12] Ko, D. C., and Kim, B. M., 2000, "Development of an Analytical Scheme to Predict the Need for Tool Regrinding in Shearing Processes," Int. J. Mach. Tools Manuf., **40**, pp. 1329–1349.
[13] Gojiaerts, A. M., Govaert, L. E., and Baaijents, F. P. T., 2000, "Prediction of Ductile Fracture in Metal Blanking," ASME J. Manuf. Sci. Eng., **122**, pp. 476–483.
[14] Pyttel, T., Ralf, J., and Hoogen, M., 2000, "A Finite Element Based Model for the Description of Aluminum Sheet Blanking," Int. J. Mach. Tools Manuf., **40**, pp. 1993–2002.
[15] Samuel, M., 1998, "FEM Simulations and Experimental Analysis of Parameters of Influence in the Blanking Process," J. Mater. Process. Technol., **84**, pp. 97–106.
[16] Goijaerts, A. M., and Govaert, L. E., 2002, "Experimental and Numerical Investigation on the Influence of Process Speed on the Blanking Process," ASME J. Manuf. Sci. Eng., **124**, pp. 416–419.
[17] Kuo, R. J., 2000, "Multi-Sensor Integration for On-Line Tool Wear Estimation Through Artificial Neural Networks and Fuzzy Neural Network," Journal of Engineering Applications of Artificial Intelligence, **13**, pp. 249–261.
[18] Fraticelli, B. M. P., Lehtihet, E. A., and Cavalier, T. M., 1999, "Tool-Wear Effect Compensation Under Sequential Tolerance Control," International Journal of Production Research, **37**(3), pp. 639–651.
[19] Choudhury, S. K., and Kishore, K. K., 2000, "Tool Wear Measurement in Turning Using Force Ratio," Int. J. Mach. Tools Manuf., **40**, pp. 899–909.
[20] Lee, W. B., Cheung, C. F., Chiu, W. M., and Chan, L. K., 1997, "Automatic Supervision of Blanking Tool Wear Using Pattern Recognition Analysis," Int. J. Mach. Tools Manuf., **37**(8), pp. 1079–1095.
[21] Kalpakjian, S., 1984, *Manufacturing processes for engineering materials*, Addison-Wesley Publishing Company, p. 391.
[22] Luo, S. Y., 1997, "Studies on the Wear Conditions and the Sheared Edges in Punching," Wear, **208**, pp. 81–90.

Characteristics of Heat Transfer During Machining With Rotary Tools

H. A. Kishawy and A. G. Gerber

Mechanical Engineering Department, University of New Brunswick, Fredericton, NB E3B 5A3 Canada

In this paper a model is developed to analyze heat transfer and temperature distribution resulting during machining with rotary tools. The presented model is based on a finite-volume discretization approach applied to a general conservation of energy statement for the rotary tool and chip during machining. The tool rotational speed is modeled and its effect on the heat partitioning between the tool and the chip is investigated. The model is also used to examine the influence of tool speed on the radial temperature distribution on the tool rake face. A comparison between the predicted and previously measured temperature data shows good agreement. In general the results show that the tool-chip partitioning is influenced dramatically by increasing the tool rotational speed at low to moderate levels of tool speed. Also, there is an optimum tool rotational speed at which further increase in the tool rotational speed increases the average tool temperature.
[DOI: 10.1115/1.1643080]

1 Introduction

The high cutting temperatures, generated during machining, cause damage on the machined surface and accelerate diffusion tool wear. In addition it can cause thermal softening of the tool tip leading to plastic deformation and hence alters the accuracy of the produced parts. Considerable efforts have been made to study the heat generation during machining using theoretical models as well as experimental methods [1–12]. The adverse effect of high temperature on the tool can be reduced by removing the heat generated through a cooling cycle as in interrupted cutting. Shaw et al. [13] presented a novel approach for accomplishing this by using a cutting edge in the form of a disk that rotates around its center. The circular cutting edge allows for a continuously fresh portion of the edge to be engaged with the workpiece. This work provided the basic concept for further investigations by other researchers [14–19]. There were no attempts, at least in the open literature, to

Copyright © 2004 by ASME

Table 1 Thermal properties of the tool and workpiece material

	ρ (kg/m^3)	c_p (J/kg K)	k (W/mK)
Tool (High speed steel)	8600	360	30
Workpiece (Plain carbon steel)	7850	486	52

model the effect of the tool rotational speed on the temperature generated in machining with rotary tools. In this paper a heat transfer model is presented and used to examine the influence of tool rotational-speed on the heat partitioning and temperatures in the tool.

2 Heat Transfer Model of the Rotary Tool

In the presented analysis it is assumed that the chip formation takes place along a thin shear zone and the formed chip moves as a rigid body along the rake face of the tool. The heat generation associated with the shear zone is calculated based on the analysis presented previously [11]. Table 1 shows the thermal properties of the materials that were used in this investigation. The convection heat transfer coefficient used was 100 W/m^{2}K (dry machining) and the ambient temperature was 20°C. Although the thermal properties are temperature dependent in this investigation the effect of temperature is ignored for simplicity.

One of the primary benefits of the rotary tool is the potential for carrying out the cutting process at a lower tool temperature. In light of this it becomes important to obtain a clear understanding of the heat transfer characteristics of the rotary tool. In developing a framework for the mathematical models presented in this paper, it is considered that the chip is moving at a speed, V_c, and in contact with the tool over a frictional area, A_{c1}. The rotary tool is spinning with an angular velocity ω_t.

The conservation equation describing the movement of energy within the body of the chip can be described by:

$$\frac{\partial}{\partial t}(\rho J\phi)_c + \frac{\partial}{\partial \varepsilon}(\rho JU\phi)_c + \frac{\partial}{\partial \eta}(\rho JV\phi)_c + \frac{\partial}{\partial \zeta}(\rho JW\phi)_c$$

$$= \frac{\partial}{\partial \varepsilon}\left(J\frac{k_c}{c_c}\left(g_{11}\frac{\partial \phi_c}{\partial \varepsilon}\right)\right) + \frac{\partial}{\partial \eta}\left(J\frac{k_c}{c_c}\left(g_{22}\frac{\partial \phi_c}{\partial \eta}\right)\right)$$

$$+ \frac{\partial}{\partial \zeta}\left(J\frac{k_c}{c_c}\left(g_{33}\frac{\partial \phi_c}{\partial \zeta}\right)\right) + S_c \qquad (1)$$

where ϕ is the specific internal energy, ρ the density of the material, k the thermal conductivity and c specific heat. To account for the effect of the heat generation in the primary shear zone, a heat source S_c is included. Similarly, the conservation equation describing the movement of energy within the body of the tool is given by the same equation with subscripts c (chip) changed to t (tool), and the heat source $S_t = 0$. These equations account for both the conduction and advection of energy in a moving mass, and are cast in generalized coordinates (ε, η, ζ) to account for the geometric differences between the chip and tool (i.e. rectangular versus cylindrical shapes). A description of the transformation metrics, g_{11}, g_{22} and g_{33}, the contravariant velocities U, V, and W, along with the Jacobian of the transformation, J, are provided in Ref. [20].

The chip and tool interact through a common interface, where the heat generated along the interface, S_{ct}, is transferred by conduction into the chip and tool. The value of S_{ct}, defined as a heat rate per unit area, depends on the relative velocity between the chip and tool, V_{rel}, and the friction force F_{ct}. Choosing the η transformed coordinate (the coordinate surface along which the
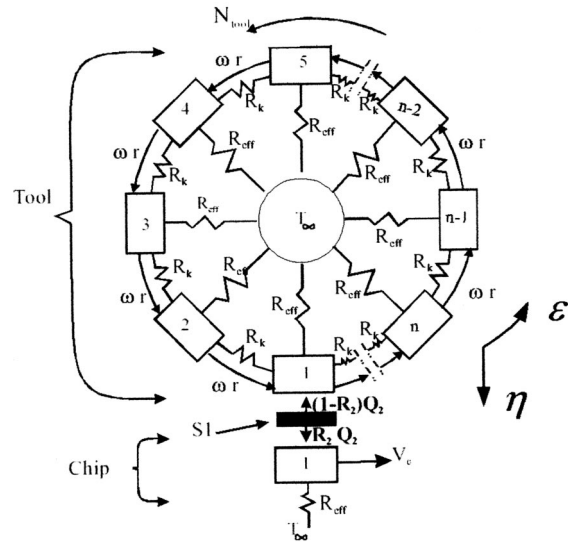

Fig. 1 A simplified model for the tool, the chip, and the chip-tool interface

friction face is applied) the conservation of surface flux at the interface yields the following:

$$\frac{k_t}{c_t}\left(Jg_{22}\frac{\partial \phi_t}{\partial \eta}\right) + \frac{k_c}{c_c}\left(Jg_{22}\frac{\partial \phi_c}{\partial \eta}\right) = J(\eta_x + \eta_y + \eta_z)S_{ct} \qquad (2)$$

where the subscripts t and c refer to the tool and chip side of the interface respectively. The metrics η_x, η_y and η_z are described in [20] and the term $J(\eta_x + \eta_y + \eta_z)$ is equal to the area A_{c1}. The ability of the heat to be moved away from the friction zone depends on the heat transfer characteristics of the chip and the tool, and the movement of heated material away from the friction zone. A special characteristic of the rotary tool is that the heated material is continuously moved away for cooling and returned to the cutting zone to potentially acquire more heat. To examine the unique features of the rotary tool, two levels of application of Eq. (2) and (3) are considered.

In the first application a simplified discrete model is derived providing a means to evaluate the influence of tool rotational speed and cutting speed on important cutting parameters. These parameters include the heat partitioning coefficient, R_2, the chip/tool interface temperature, T_{ct}, and the average tool temperature T_{ta}. This model, intended for parametric studies, includes thermal interactions between the chip, chip-tool interface, and the rotary tool and the surroundings. A schematic of the model, showing how the control-volumes in the analysis are linked, is shown in Fig. 1. The application of Eqs. (2) and (3) with appropriate simplifications, results in a predicted circumferential temperature distribution in the tool, the chip-tool interface and chip temperatures. The required simplifications are described in [20]

The second level of application involves a 3-D discrete model of the rotary tool, and provides a means to examine in detail the temperature distributions in the tool as a function of rotational speed. For the subsequent development of the discrete equation set, Eq. (1) is discretized using a finite-volume discretization [21]. The coordinate transformation terms are retained to allow for flexibility in developing equation sets for different geometry. Following integration over a control-volume of dimension $\Delta \varepsilon = 1$, $\Delta \eta = 1$, and $\Delta \zeta = 1$, and using Gauss's theorem to convert volume integrals to surface integrals for the convective and diffusive terms, the conservation equation for the chip and tool becomes:
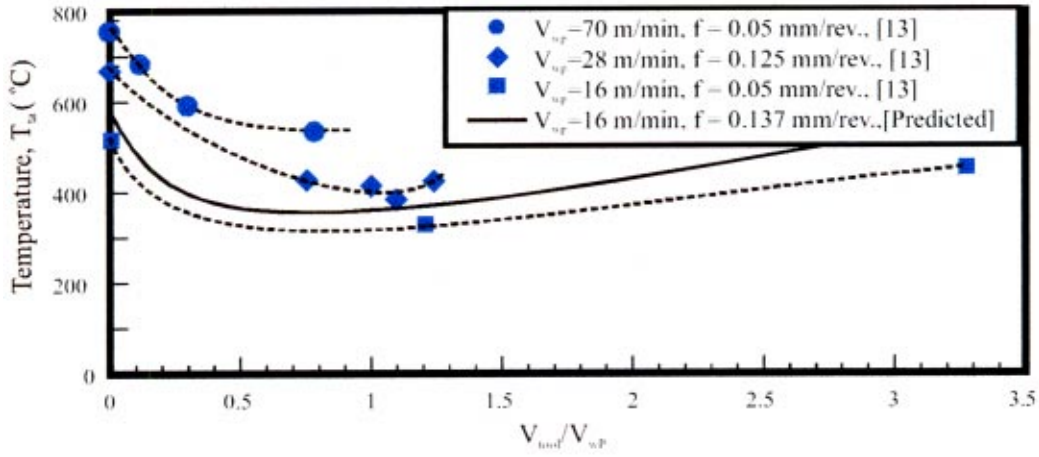
Fig. 2 Measured and predicted temperatures at different velocity ratio

$$\frac{(\rho J)_c}{\Delta t}(\phi_{ijk} - \phi_{ijk}^o)_c + (\Omega_e - \Omega_w)_c + (\Omega_n - \Omega_s)_c + (\Omega_t - \Omega_h)_c = S_c \quad (3a)$$

$$\frac{(\rho J)_t}{\Delta t}(\phi_{ijk} - \phi_{ijk}^o)_t + (\Omega_e - \Omega_w)_t + (\Omega_n - \Omega_s)_t + (\Omega_t - \Omega_b)_t = 0 \quad (3b)$$

where the control-volume surface fluxes, Ω (defined at the east (*e*), west (*w*), north (*n*), south (*s*), top (*t*) and bottom (*b*) faces of the control-volume) include the transport of energy (advection) and thermal diffusion. The transient term disappears in the steady-state but is retained for generality, and acts as a means for relaxing the solution during iterative refinement. Considering only the *e*-face, as all other faces follow a similar development, the surface flux is:

$$\Omega_e = \rho J U \phi_e - \frac{k}{c} J g_{11} \frac{\partial \phi}{\partial \varepsilon} \quad (4)$$

In the general 3-D case the control-volume, with internal energy level ϕ_{ijk}, is surrounded by six adjacent control-volumes located to the east (ϕ_{i+1jk}), west (ϕ_{i-1jk}), north (ϕ_{ij+1k}), south (ϕ_{ij-1k}), top (ϕ_{ijk+1}) and bottom (ϕ_{ijk-1}). At the *e*-face (with similar developments for all other faces) the value of ϕ_e, which must be interpolated using adjacent control-volume values of ϕ (i.e., ϕ_{i+1jk} and ϕ_{ijk} for the *e*-face), depends on the relative strengths of the convective and diffusive fluxes and is approximated by the power law function [21]:

$$\Omega_e = F_e \left(\phi_{ijk} + \frac{(1 - 0.1|P.Pe|)^5}{Pe}(\phi_{i+1,jk} - \phi_{ijk}) \right) \quad (5)$$

where *Pe* is the Peclet number.

Equation (5) can be substituted into Eq. (3), with similar substitutions for the other faces (i.e. *w-s-n-t-b*), to arrive at conservation equation for the control-volume in terms of its internal energy, ϕ_{ijk}, and the surrounding nodal internal energies ϕ_{i+1kj}, ϕ_{i-1jk}, ϕ_{ij+1k}, ϕ_{ij-1k}, ϕ_{ijk+1} and ϕ_{ijk-1} for the 3-D case, and ϕ_i, ϕ_{i-1} for simplified cases where temperatures vary in one grid dimension only. The temperature is determined from the internal energy using specific heat information for the material.

The discrete equation for the chip-tool interface is obtained by a finite-difference approximation of the gradient terms (in Eq. (2)) on each side of the interface, using $\Delta \eta = 1/2$, one obtains:

$$\left(\frac{k_t}{c_t} + \frac{k_c}{c_c} \right) \phi_{ct} - \left(\frac{k_c}{c_c} \right) \phi_j - \left(\frac{k_t}{c_t} \right) \phi_i = \frac{J}{2g_{22}}(\eta_x + \eta_y + \eta_z)S_{ct} \quad (6)$$

where ϕ_{ct} is the interface energy level, and ϕ_i and ϕ_j the tool and chip internal energy levels respectively.

Equations (3) and (6) can be used to develop the discrete equation set for the level one and level two applications, however, specific features relating to boundary conditions, chip-tool interaction, and assumptions can be found in [20], due to space constraints.

3 Results and Discussions

Figure 2 shows the predicted effect of the tool-cutting velocity ratio on tool temperature. Also experimentally measured temperature data is reproduced from Shaw et al. [13]. Their reported data is only of value in showing trends in the temperature of the rotary tool in conjunction with changes in feed and cutting speed. The trends in Fig. 2 indicate that with increasing tool-cutting velocity ratio the tool temperature is rapidly reduced. This behavior is more pronounced at lower values of cutting speed V_w. For each combination of cutting speed and feed there is an optimum tool-
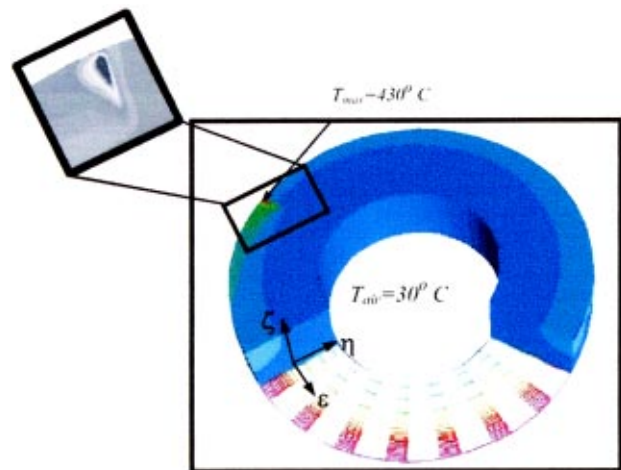

Fig. 3 Typical Temperature Distribution in a 3-D rotary tool with applied velocity field shown (T_{max}=430 C, T_{min}=30 C, *contour intervals of* ΔT=25 C)
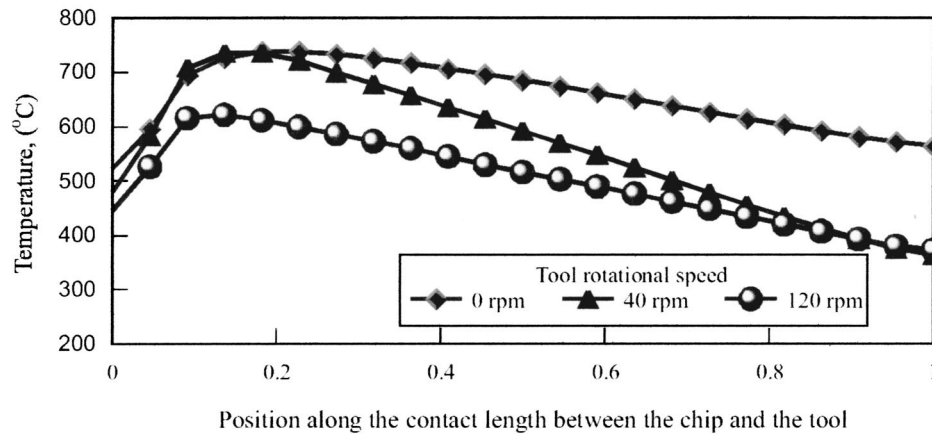
Fig. 4 Effect of tool speed on the temperature distribution on the rake face

cutting velocity ratio at which the average tool temperature is a minimum. In general the chip, because it always involves continuous movement of workpiece material away from the cutting zone, carries away a majority of the heat generated in the cutting process at typical cutting speeds. In a similar way, the added motion of the rotary tool removes additional heat that should have a combined effect of reduced tool temperatures. However, since the tool material continuously returns to the cutting zone there should be a limit to the improved cooling performance.

An interesting feature of Fig. 2 is that the minimum temperature occurs at a velocity ratio much higher than practical applications of self-propelled tools [19]. However, it should be stated that in a driven rotary tool a higher velocity ratio can be utilized to operate nearer the minimum tool temperature. These results suggest that the improved performance of a self-propelled tool is primarily due to the longer cutting edge and not the temperature reduction. The driven tool shows the potential of achieving both the optimal reduced tool temperature along with the increased cutting edge length.

Figure 3 shows the typical temperature distribution of the rotary tool at a tool rotational speed of 120 rpm. Three tool rotational speeds of 0, 40 and 120 rpm are used to produce the temperature distributions on the tool rake face shown in Fig. 4. As can be seen, increasing the tool rotational speed reduces the peak temperature as well as the bulk tool temperature. However, the reduction of the bulk tool temperature is more pronounced at higher values of tool rotational speed. In addition, the position of the peak temperature value is shifted toward the cutting edge at higher tool-rotational speeds.

4 Conclusions

A finite-volume heat transfer model has been developed and used to study the heat transfer characteristics of rotary tools. The study has shown that increasing the tool-cutting velocity ratio reduces the average tool temperature to a minimum value. Further increase of the velocity ratio increases the average tool temperature. However, the model indicates that a lower tool temperature is obtained at a velocity ratio much higher than that utilized in practice for self-propelled rotary tools. This suggests that the self-cooling feature is not the prime reason for longer tool life, but rather the longer cutting edge in the rotary tool.

References

[1] Kops, L., and Arenson, M., 1999, "Determination of Convective Cooling Conditions in Turning," CIRP Ann., **48**, pp. 47–52.
[2] Boothroyed, G., 1963, "Temperatures in Orthogonal Metal Cutting," Proc. Inst. Mech. Eng., **177**, pp. 789–810.
[3] Tay, A. O., Stevenson, M. G., Davis, G., and Oxley, P. L., 1976, "A Numerical Method for Calculating Temperature Distributions in Machining from Force and Shear Angle Measurements," Int. J. Mach. Tool Des. Res., **16**, pp. 335–349.
[4] Ng, E. G., Aspinwall, D. K., Brazil, D., and Monaghan, J., 1999, "Modelling of Temperature and Forces When Orthogonally Machining Hardened Steel," Int. J. Mach. Tools Manuf., **39**, pp. 885–903.
[5] Kottenstette, J. P., 1986, "Measuring Tool/Chip Interface Temperatures," ASME J. Eng. Ind., **108**, pp. 101–104.
[6] Ostafiev, V., Kharkevich, A., Weinert, K., and Ostafiev, S., 1999, "Tool Heat Transfer in Orthogonal Metal Cutting," ASME J. Manuf. Sci. Eng., **121**, pp. 541–549.
[7] Kato, S., Yamaguchi, K., Watanabe, Y., and Hiraiwa, Y., 1976, "Measurements of Temperature Distribution Within Tool Using Powders of Constant Melting Point," ASME J. Eng. Ind., **98**, pp. 607–613.
[8] Yen, D. W., and Wright, P. K., 1986, "A Remote Temperature Sensing Technique for Estimating The Cutting Interface Temperature Distribution," ASME J. Eng. Ind., **108**, pp. 252–263.
[9] Wright, P. K., McCormick, S. P., and Miller, T. K., 1980, "Effect of Rake Face Design on Cutting Tool Temperature Distributions," ASME J. Ind., **102**, pp. 123–128.
[10] Stephenson, D. A., 1991, "Assessment of Steady-State Metal Cutting Temperature Models Based on Simultaneous Infrared and Thermocouple Data," ASME J. Eng. Ind., **113**, pp. 121–128.
[11] Venuvinod, P. K., and Lau, W. S., 1986, "Estimation of Rake Temperatures in Free Oblique Cutting," Int. J. Mach. Tool Des. Res., **26**, pp. 1–4.
[12] Chao, B. T., and Trigger, K. J., 1958, "Temperature Distribution at Tool-Chip and Tool-Work Interface In Metal Cutting," Trans. ASME, **80**, pp. 311–320.
[13] Shaw, M. C., Smith, P. A., and Cook, N. A., 1952, "The Rotary Cutting Tool," Trans. ASME, **74**, pp. 1065–1076.
[14] Armarego, E. J. A., Karri, V., and Smith, A. J. R., 1994, "Fundamental Studies of Driven and Self-Propelled Rotary Tool Cutting Processes-I. Theoretical Investigation," Int. J. Mach. Tools Manuf., **34**(6), pp. 785–801.
[15] Venuvinod, P. K., Lau, W. S., and Reddy, P. N., 1981, "Some Investigation in Machining With Driven Rotary Tools," ASME J. Eng. Ind., **103**, pp. 469–477.
[16] Thomas, R. M., and Lawson, R. L., 1967, "Applications of Rotary Turning Tool," *17th International MATADOR Conf.*, Sep. 20–24, pp. 125–131.
[17] Chen, P., 1992, "High-Performance Machining of SiC Whisker-Reinforced Aluminum Composite by Self-Propeeled Rotary Tools," CIRP Ann., **41**, pp. 59–62.
[18] Kishawy, H. A., Shawky, A. M., and Elbestawi, M. A., 2001, "Assessment of Self-Propelled Rotating Tools During High Speed Milling," SME, *Proceeding of the 4th International Machining & Grinding Conference*, May 7–10, Troy, Michigan, pp. 1–11.
[19] Kishawy, H. A., and Wilcox, J., 2002, "Tool Wear and Chip Formation During Hard Turning with Self-Propelled Rotary Tools," To appear in the Int. J. Mach. Tools Manuf.
[20] Kishawy, H. A., and Gerber, A. G., 2001, "A Model for the Tool Temperature During Machining With a Rotary Tool," *International Mechanical Engineering Congress and Exposition Symposium on Fundamental Issues in Machining*, Volume 3, ECE2001/MED-23312, pp. 1–10.
[21] Patankar, S. V., 1980, *Numerical Heat Transfer and Fluid Flow*, Hemisphere, McGraw-Hill.

A Quantitative Sensitivity Analysis of Cutting Performances in Orthogonal Machining with Restricted Contact and Flat-Faced Tools

Ning Fang

Assistant Professor,
Mem. ASME,
Department of Mechanical and Aerospace Engineering,
Utah State University, Logan, Utah 84322-4130
e-mail: ning.fang@usu.edu
URL: http://www.mae.usu.edu/faculty/nfang

This paper presents a new quantitative sensitivity analysis of cutting performances in orthogonal machining with restricted contact and flat-faced tools, based on a recently developed slip-line model. Cutting performances are comprehensively measured by five machining parameters, i.e., the cutting forces, the chip back-flow angle, the chip up-curl radius, the chip thickness, and the tool-chip contact length. It is demonstrated that the percentage of contribution of tool-chip friction to the variation of cutting performances depends on different types of machining operations. No general conclusion about the effect of tool-chip friction should be made before specifying a particular type of machining operation and cutting conditions. [DOI: 10.1115/1.1643081]

1 Introduction

Sensitivity analysis investigates how the variation in outputs of a model can be apportioned, qualitatively or quantitatively, to different sources of variation [1]. Sensitivity analysis of cutting performances is one of the effective approaches to studying the basic mechanism of chip formation in machining. It identifies the most important factors governing changes in cutting performances and provides a solid foundation for the optimization of practical machining applications. Sensitivity analysis has been widely employed in robust design of machine tool structures and metal forming research. However, it has not received significant attention in machining research. So far, only a very few studies can be found from the published literature [2–3]. Moreover, most of them employed the numerical approach and were concentrated in thermal aspects of machining processes.

A new sensitivity analysis for machining with restricted contact (RC) and flat-faced tools is presented in this paper to quantitatively study the effect of the state of stresses in the plastic deformation region, tool geometry, and cutting conditions on the variation of cutting performances. The cutting forces, chip back-flow angle, chip up-curl radius, chip thickness, and tool-chip contact length are employed to comprehensively measure cutting performances. A series of new insights into the basic mechanism of chip formation, especially tool-chip friction, have been obtained.

2 Model of Chip Formation

A recently developed slip-line model for RC machining [4] is employed in the present study. Involving a convex upward shear plane and four slip-line angles, the model [4] takes into account both the chip up-curling and back-flow effects and incorporates six other slip-line models previously developed for machining during the last six decades as special cases. The mathematical

formulation of the model is based on Dewhurst and Collins' matrix technique for numerically solving slip-line problems [5]. A good agreement has been found between theory and experiments through extensive cutting tests covering a wide range of cutting conditions [6].

Inputs of the model [4] include: (1) the hydrostatic pressure ratio P_A/k, where P_A is the hydrostatic pressure and k is the material shear flow stress; (2) the frictional shear stress ratio τ/k, which governs tool-chip friction on the tool rake face, (3) the tool-chip contact length ratio t_1/h, where t_1 is the undeformed chip thickness and h is the land length of the tool; and (4) the tool primary rake angle γ_1. The model [4] predicts a number of machining parameters, including (1) the cutting forces (F_c/kt_1w and F_t/kt_1w, where F_c is the cutting force, F_t is the thrust force, and w is the width of cut; (2) the chip back-flow angle η_b; (3) the chip up-curl radius R_u; and (4) the chip thickness t_2. The model [4] can also be employed to study chip formation in machining with flat-faced tools. In this latter case, the model [4] turns into exactly the same as Dewhurst's model [7]. Both models provide the same theoretical solutions to flat-faced tool machining.

3 Sensitivity Analysis of Cutting Performances

The accuracy of sensitivity analysis of cutting performances depends not only on a reliable (experimentally validated) model of chip formation, but also on the use of an effective mathematical analysis technique. In this paper, Friedman's model [8] of multivariate adaptive regression spline is incorporated into the slip-line models [4,7] to perform sensitivity analysis. Friedman's model [8] takes the form of an expansion in product spline basis functions, where the number of basis functions and the parameters associated with each one (product degree and knot locations) are automatically determined by the input data. It provides the information on the relative importance level of input variables of the model, or the percentage of contribution of input variables to the variation of cutting performances. At present, a computer software package developed from Friedman's model [8] is commercially available [9]. A free demo program that teaches how to use the software to perform sensitivity analysis is also available [9].

Table 1 lists variations of input variables of the two slip-line models [4,7]. These variations cover a wide range of cutting conditions, especially a wide range of tool-chip frictional conditions. The predicted values of cutting forces, chip back-flow angle, etc., also locate within a very wide range. It should be noted that only theoretically admissible combinations of input variables [4] given in Table 1 were employed in sensitivity analysis.

Figures 1 and 2 show the sensitivity analysis of five cutting performance measures. The vertical axes in Figs. 1 and 2 show the relative importance level of input variables of the slip-line model, or the percentage of contribution of input variables to the variation of cutting performance measures. The percentage of contribution of combined interaction between input variables was found negligible; therefore, it is not included in Figs. 1 and 2. Table 2 summarizes the major findings from Figs. 1 and 2, which are analyzed in detail as follows.

3.1 Sensitivity Analysis of Cutting Forces. As seen from Fig. 1, the tool rake angle γ_1 is the most important variable governing the variation of cutting forces, especially the thrust force F_t/kt_1w. Jawahir [10] has experimentally demonstrated the close relationship between the tool rake angle and the thrust force. The tool-chip contact length ratio t_1/h and tool-chip friction τ/k play the second important role in RC machining and flat-faced tool machining, respectively. The effect of tool-chip friction τ/k on the cutting force F_c/kt_1w is not significant in RC machining. The effect of hydrostatic pressure P_A/k can be neglected almost completely in both types of machining operations.

3.2 Sensitivity Analysis of Chip Back-Flow Angle in RC Machining. It can be seen from Fig. 2(a) that in the decreasing order of relative importance, variables governing the variation of

Table 1 Input variables of the two slip-line models

Input variables	RC machining (Fang et al.'s model [4])	Flat-faced tool machining (Dewhurst's model [7])
Hydrostatic pressure ratio P_A/k	0.75, 0.79, 0.83, 0.87, 0.91, 0.95	0.75, 0.77, 0.79, 0.81, 0.83, 0.85, 0.87, 0.89, 0.91, 0.93, 0.95
Frictional shear stress ratio τ/k	0.65, 0.71, 0.77, 0.83, 0.89, 0.95	0.65, 0.68, 0.71, 0.74, 0.77, 0.80, 0.83, 0.86, 0.89, 0.92, 0.95
Tool-chip contact length ratio t_1/h	0.80, 0.86, 0.96, 1.04, 1.12, 1.20	Not applicable
Tool primary rake angle γ_1	−9 deg, −3 deg, 3 deg, 9 deg, 15 deg	−9 deg, −3 deg, 3 deg, 9 deg, 15 deg
Total number of combinations of input variables	$6\times6\times6\times5=1080$	$12\times12\times5=720$
Total number of theoretically admissible combinations of input variables	824	612

chip back-flow angle η_b are the tool-chip contact length ratio t_1/h, tool-chip friction τ/k, and the hydrostatic pressure P_A/k. The effect of tool rake angle γ_1 can be neglected. Jawahir [10] has also experimentally demonstrated the strong relationship between η_b and t_1/h.

3.3 Sensitivity Analysis of Tool-Chip Contact Length in Flat-Faced Tool Machining. Figure 2(a) shows that the variation of tool-chip contact length l_n is sensitive to both the tool rake angle γ_1 and tool-chip friction τ/k. On the other hand, the effect of hydrostatic pressure P_A/k can be neglected.

3.4 Sensitivity Analysis of Chip Up-Curl Radius. Figure 2(b) clearly illustrates that the hydrostatic pressure P_A/k is the only variable dominating the variation of chip up-curl radius R_u in RC machining. It is also the most important variable governing the variation of R_u in flat-faced tool machining. If P_A/k takes its maximum permissible value of 1.0, straight chip formation involving infinite chip up-curl radius will be generated. Dewhurst [7] also demonstrated the strong dependence of R_u on P_A/k. Tool-chip friction τ/k plays the second important role in affecting R_u in flat-faced tool machining, but it has almost no effect in RC machining. The effect of tool rake angle γ_1 on the chip up-curl radius R_u is not significant.

3.5 Sensitivity Analysis of Chip Thickness. Figure 2(c) shows that in RC machining, the most important variable dominating the variation of chip thickness t_2 is the tool-chip contact length ratio t_1/h. The hydrostatic pressure P_A/k plays the second important role. In flat-faced tool machining, the important variables governing the variation of t_2 include the tool rake angle γ_1 and tool-chip friction τ/k.

3.6 Effect of Tool-Chip Friction in Machining. Table 2 and Figs. 1 and 2 reveal a hidden rule that has not yet been well recognized, i.e., the effect of an input variable of machining operations on cutting performances depends on a particular type of machining operation and cutting conditions. Let's take tool-chip friction τ/k on the tool rake face as an example. Tool-chip friction is one of the two bottleneck problems in the present stage of machining research worldwide. The importance of tool-chip friction in machining has long been recognized, with many statements having been made. For example, tool-chip friction always plays a significant (central) role in affecting cutting forces. Unfortunately, a statement like this is a typical *incomplete* understanding of tool-chip friction. In some machining cases, the statement is correct. In other cases, it is not.

Table 2 and Fig. 1 clearly show that tool-chip friction τ/k does have a significant effect on the cutting forces (31.3% on F_c/kt_1w and 23.13% on F_t/kt_1w) in flat-faced tool machining; however, its effect on the cutting forces (1.53% on F_c/kt_1w and 7.48% on F_t/kt_1w) is negligible in RC machining. Even in the same type of RC machining, tool-chip friction τ/k has different effects on different cutting performance measures. For example, it has a negligible effect on the cutting forces but has an important effect (25.15%) on the chip back-flow angle as shown in Fig. 2(a). Therefore, the effect of tool-chip friction actually depends on a particular type of machining operation and a particular cutting performance measure.

The opposite effects of hydrostatic pressure P_A/k on the chip thickness t_2 in RC and flat-faced tool machining, and the opposite effects of tool rake angle γ_1 on t_2 in these two types of machining operations provide two additional examples. Figure 2(c) shows

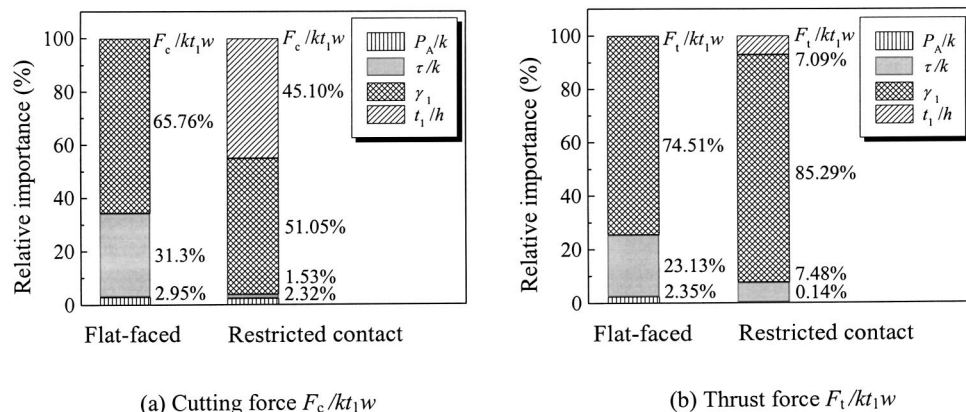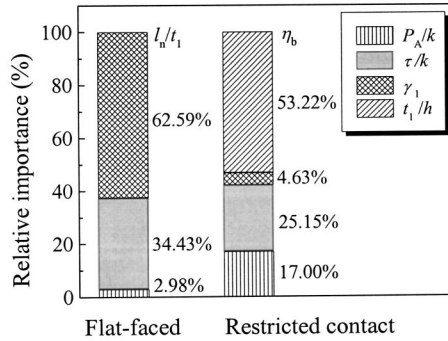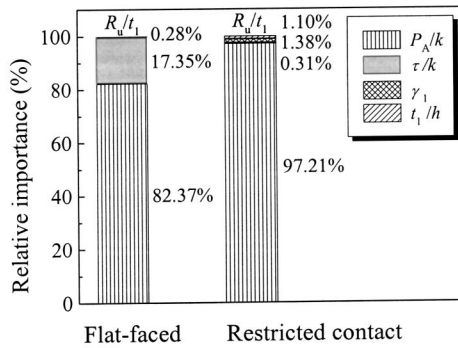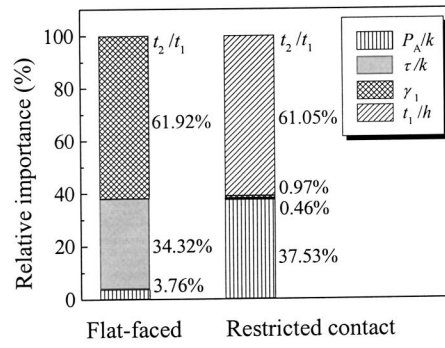(a) Cutting force F_c/kt_1w (b) Thrust force F_t/kt_1w

Fig. 1 Sensitivity analysis of cutting forces

(a) Chip back-flow angle η_b and tool-chip contact length l_n/t_1

(b) Chip up-curl radius R_u/t_1

(c) Chip thickness t_2/t_1

Fig. 2 Sensitivity analysis of chip back-flow angle, tool-chip contact length, chip upcurl radius, and chip thickness

that the hydrostatic pressure P_A/k plays a significant role (37.53%) in affecting t_2 in RC machining; however, its effect on t_2 (3.76%) in flat-faced tool machining can be neglected. Figure 2(c) shows that the tool rake angle γ_1 has almost no effect (0.97%) on t_2 in RC machining; however, it plays the most important role (61.92%) in affecting t_2 in flat-faced tool machining.

To explain the observations made above, we need to consider both tool geometry and the chip deformation mechanism. Let's still take tool-chip friction as an example. In flat-faced tool machining, the size of the secondary shear zone on the tool rake face is mainly governed by tool-chip friction due to a relatively large length of the natural tool-chip contact. As a result, the cutting

Table 2 Effect of input variables of the model on the variation of cutting performances

Influential variables	In RC machining	In flat-faced tool machining	In RC machining	In flat-faced tool machining
	Has significant effect on the following cutting performance measures		Has negligible effect on the following cutting performance measures	
P_A/k	R_u/t_1 t_2/t_1 η_b	R_u/t_1	F_c/kt_1w F_t/kt_1w	F_c/kt_1w F_t/kt_1w l_n/t_1 t_2/t_1
τ/k	η_b	F_c/kt_1w F_t/kt_1w l_n/t_1 t_2/t_1 R_u/t_1	F_c/kt_1w F_t/kt_1w R_u/t_1 t_2/t_1	No
t_1/h	F_c/kt_1w	Not applicable	F_t/kt_1w η_b R_u/t_1 t_2/t_1	Not applicable
γ_1	F_c/kt_1w F_t/kt_1w	F_c/kt_1w F_t/kt_1w l_n/t_1 t_2/t_1	η_b R_u/t_1 t_2/t_1	R_u/t_1

forces are highly sensitive to tool-chip friction. However, in RC machining, the chip only contacts tool land over a restricted length, which can be far less than the natural tool-chip contact length. Even a significant variation in tool-chip friction τ/k does not cause a profound change in the size of the secondary shear zone, or a significant change in the cutting forces. The opposite effects of tool-chip friction further imply that in flat-faced tool machining, the cutting forces can be decreased by reducing tool-chip friction, such as by employing tool coatings and lubricants (cutting oils); nevertheless, the cutting forces cannot be significantly decreased by reducing tool-chip friction in machining with a restricted contact cutaway tool. Chiffre [11] has reported this latter phenomenon in RC machining experiments with different types of cutting oils.

4 Concluding Remarks

The following summarizes the major new findings made from this paper:

1. The tool rake angle γ_1 is the most important variable governing the variation of cutting forces, especially the thrust force, in both RC and flat-faced tool machining.
2. The tool-chip contact length ratio t_1/h plays the most important role in affecting the variation of chip back-flow angle in RC machining.
3. The hydrostatic pressure P_A/k dominates the variation of chip up-curl radius in both types of machining operations.
4. The most important parameter dominating the variation of chip thickness is the tool-chip contact length ratio t_1/h in RC machining, or the tool rake angle γ_1 in flat-faced tool machining.
5. The variation of tool-chip contact length is sensitive to both the tool rake angle γ_1 and tool-chip friction τ/k in flat-faced tool machining.

6. The percentage of contribution of tool-chip friction to the variation of cutting performances depends on different types of machining operations. No general conclusion about the effect of tool-chip friction should be made before specifying a particular type of machining operation and cutting conditions. This conclusion clarifies a long-existing, incomplete understanding of the effect of tool-chip friction in machining.

References

[1] Saltelli, A., Chan, K., and Scott, E. M., 2000, *Sensitivity Analysis*, John Wiley & Sons Limited, Chichester, England.
[2] Leshock, C. E., Kim, J. N., and Shin, Y. C., 2001, "Plasma Enhanced Machining of Inconel 718: Modeling of Workpiece Temperature with Plasma Heating and Experimental Results," Int. J. Mach. Tools Manuf., **41**, pp. 877–897.
[3] Chan, C. L., and Chandra, A., 1991, "BEM Approach to Thermal Aspects of Machining Processes and Their Design Sensitivities," Appl. Math. Model., **15**, pp. 562–575.
[4] Fang, N., Jawahir, I. S., and Oxley, P. L. B., 2001, "A Universal Slip-Line Model with Non-Unique Solutions for Machining with Curled Chip Formation and a Restricted Contact Tool," Int. J. Mech. Sci., **43**, pp. 557–580.
[5] Dewhurst, P., and Collins, I. F., 1973, "A Matrix Technique Constructing Slip-Line Field Solutions to a Class of Plane Strain Plasticity Problems," Int. J. Numer. Methods Eng., **7**, pp. 357–378.
[6] Fang, N., and Jawahir, I. S., 2002, "Analytical Predictions and Experimental Validation of Cutting Forces, Chip Thickness, and Chip Back-Flow Angle in Restricted Contact Machining Using the Universal Slip-Line Model," Int. J. Mach. Tools Manuf., **42**, pp. 681–694.
[7] Dewhurst, P., 1978, "On the Non-Uniqueness of the Machining Process," Proc. R. Soc. London, Ser. A, **360**, pp. 587–610.
[8] Friedman, J. H., 1991, "Multivariate Adaptive Regression Splines," Ann. Stat., **19**, pp. 1–67.
[9] http://www.salford-systems.com.
[10] Jawahir, I. S., 1986, "An Experimental and Theoretical Study of the Effects of Tool Restricted Contact on Chip Breaking," Ph.D. thesis, The University of New South Wales, Australia.
[11] Chiffre, L. De, 1982, "Cutting Tools with Restricted Contact," Int. J. Mach. Tool Des. Res., **22**, pp. 321–331.